Computer Modeling in Engineering & Sciences

Tech Science Press

https://doi.org/10.32604/cmes.2026.088413

ARTICLE

Physics-Guided Cascaded Neural Network with Fourier Feature Mapping for Rapid Prediction of Transient Pulsating Grouting

Weiqun Liang[1], Weiqin Xu[2], Xiaobin Chen[1,*], Yu Zhang[1], Qipei Han[1], Tiejie Xu[1] and Jiasheng Zhang[1]

[1]School of Civil Engineering, Central South University, Changsha, China
[2]School of Economics and Management, East China Jiaotong University, Nanchang, China

*Corresponding Author: Xiaobin Chen. Email: chen_xiaobin@csu.edu.cn

Received: 03 July 2026; Accepted: 08 September 2026; Published: 21 October 2026

ABSTRACT: Simulating high-frequency pulsating grouting for structural reinforcement imposes stringent time-step limitations on computational fluid dynamics (CFD), creating severe computational bottlenecks. While physics-informed neural networks (PINNs) offer promising surrogates, they face two challenges in high-frequency multiphase flows: traditional PINNs suffer from interfacial numerical dissipation and fail to track pressure peaks, whereas purely periodic activations trigger non-physical spurious oscillations in mid-to-far field regions. To overcome these, we propose a physics-guided cascaded PINN with Fourier Feature Mapping (FFM). By injecting the predicted volume of fluid (VOF) as a physical prior into the pressure network via a Sigmoid hard constraint, this dual-branch architecture decouples multi-field nonlinearities and mitigates gradient conflicts. Concurrently, a decoupled FFM-GELU strategy provides exceptional high-frequency perception, precisely capturing sharp air-grout interfaces and pressure pulsations while eradicating far-field noise. Results demonstrate the model reduces the VOF mean squared error to 6.55×10^{-5} and global pressure error to 2.87%. Posterior evaluations confirm strict mass conservation without relying on traditional full-equation soft constraints. Remarkably, the surrogate compresses physical evolution time from 2.16×10^{4} s in CFD to 6.50×10^{-3} s (6.5 ms). This acceleration of over six orders of magnitude establishes a highly efficient millisecond-level paradigm for real-time digital twins in underground engineering.

KEYWORDS: Physics-informed neural network (PINN); high-frequency pulsating grouting; multiphase flow; fourier feature mapping (FFM); cascaded architecture; surrogate model

1 Introduction

Grouting technology is a critical method for soil reinforcement, groundwater control, and the stabilization of structural foundations in underground engineering. Traditional steady-pressure displacement has obvious limitations in complex porous media and fractured rock masses; it is highly prone to inducing preferential flow paths or fingering instabilities, and often causes particle clogging at pore throats, severely restricting the transport range of multiphase flows [1]. Recently, dynamic pulsating grouting has shown immense potential [2]. By applying alternating hydrodynamic loads at the inlet, it effectively breaks the mechanical arching effect of particles, significantly enhancing the diffusion efficiency of grout in low-permeability media [3]. However, this transient variable-pressure displacement mechanism poses unprecedented challenges for the theoretical analysis and numerical solution of multiphase flows [4].

Copyright © 2026 The Authors. Published by Tech Science Press. This work is licensed under a Creative Commons Attribution 4.0 International License, which permits unrestricted use, distribution, and reproduction in any medium, provided the original work is properly cited.

To reveal the micro-hydrodynamic mechanisms of pulsating grouting, computational fluid dynamics (CFD) is widely used to solve the Navier-Stokes equations alongside multiphase flow interface tracking methods (e.g., the Volume of Fluid (VOF) method [5]). Nevertheless, simulating dynamic forced boundaries faces severe computational bottlenecks [6]. The alternating boundary pressures impose strict Courant-Friedrichs-Lewy (CFL) stability conditions on CFD solvers. To control numerical errors and prevent divergence, solvers must adopt extremely small time steps that are deeply tied to the dynamic forcing frequency. Such stringent temporal resolution requirements lead to exponentially increasing computational costs. Consequently, traditional CFD methods are difficult to apply directly to the real-time state synchronization requirements of predictive digital twins for underground structural reinforcement processes [7,8]. There is an urgent need to develop surrogate models combining high computational efficiency with high physical fidelity to enhance traditional CFD [9–11].

In recent years, physics-informed neural networks (PINNs) [12,13] have demonstrated immense potential as efficient surrogate models for complex fluid dynamics [14]. By embedding partial differential equations into the loss function as physical soft constraints, scholars have successfully utilized PINNs for forward and inverse modeling of flow fields in porous media [15–18]. Furthermore, PINNs have been effectively applied to multiphase flow saturation prediction and interfacial instability analysis [19,20]. However, in the fields of multiphase flow and grouting diffusion, existing PINN research is predominantly limited to traditional steady-state or constant-pressure evolution scenarios. Studies on PINN surrogate models driven by dynamic pulsating pressure remain significantly insufficient.

Constructing a PINN model for dynamic variable-pressure multiphase flow faces two severe mathematical challenges. First, traditional PINNs equipped with conventional smooth activation functions (e.g., Swish or Tanh) suffer from severe "spectral bias" [21]. They inherently act as low-pass filters, failing to fit the drastic spatial step changes of the VOF gas-liquid interface (leading to severe numerical smearing) [22] and underestimating the dynamic pressure peaks, thus failing to track the high-frequency pressure pulsations. Furthermore, gradient conflicts between different physical variables in multiphase flow equations often trigger severe convergence pathologies [23–25]. To break the spectral bias, recent studies have introduced purely periodic activation functions, such as Sinusoidal Representation Networks (SIREN) [26]. However, the highly oscillatory nature of SIREN creates an extremely rugged loss landscape. When solving strongly nonlinear multiphase flows, it is highly prone to triggering severe non-physical spurious oscillations in smooth flow regions (e.g., the far-field or static phase regions), completely failing to meet the global stability requirements of multiphase flow simulations.

To explicitly overcome the aforementioned challenges of severe spectral bias, non-physical spurious oscillations, and the computational bottlenecks inherent in traditional CFD solvers, this paper proposes a novel physics-guided cascaded neural network integrated with Fourier Feature Mapping (Cascaded FFM-PINN). The original achievements formulated to address these specific difficulties are summarized as follows:

(1) Mitigation of Gradient Conflicts through a Cascaded Dual-Branch Architecture: To address the convergence pathologies induced by multi-field coupling, the proposed architecture mathematically embeds the underlying physical causality of multiphase flows. By explicitly injecting the predicted volume fraction as a physical prior into the pressure network via a Sigmoid hard constraint, this cascaded mechanism effectively decouples strong nonlinearities and ensures rapid, high-fidelity convergence within 3000 epochs.

(2) Resolution of Spectral Bias and Spurious Oscillations via a Decoupled FFM-GELU Strategy: To resolve the inherent conflict between interfacial smearing in traditional PINNs and non-physical noise in purely periodic networks, Fourier Feature Mapping (FFM) [27,28] and Gaussian Error Linear Unit (GELU) activations are synergistically implemented. FFM provides exceptional dynamic perception

to precisely track 10 Hz pulsations and localize high-gradient interfaces [29]. Concurrently, the GELU activation maintains a smooth loss landscape, fundamentally eradicating far-field numerical noise.

(3) Elimination of CFD Computational Bottlenecks via Millisecond-Level Inference: To bypass the stringent Courant-Friedrichs-Lewy stability constraints of traditional numerical solvers, a hybrid spatio-temporal sampling strategy is designed to capture transient dynamics. The fully trained surrogate model compresses the physical evolution time from 2.16×10^4 s (6.0 h) in CFD to 6.50×10^{-3} s (6.5 ms). This acceleration, exceeding six orders of magnitude, establishes a highly efficient computational baseline for real-time state reconstruction in structural digital twins [30].

(4) Verification of Physical Rigor through Posterior Validation: To ensure the physical reliability of the data-driven surrogate, comprehensive posterior residual analyses are conducted. These evaluations prove that the model strictly satisfies mass conservation and fluid dynamics governing equations without relying on explicit full partial differential equations (PDE) constraints. Furthermore, systematic sensitivity analyses on sampling ratios and loss weights confirm the exceptional global robustness of the proposed framework.

2 Methodology

2.1 Physical Model and Governing Equations

This study investigates the high-frequency pulsating grouting process. This process fundamentally involves the transient multiphase dynamic behavior of grout displacing air within a porous medium. As illustrated in Fig. 1, the geometric model for the computational fluid dynamics (CFD) simulation is defined as a three-dimensional (3-D) cubic soil domain with dimensions of $1\,\text{m} \times 1\,\text{m} \times 1\,\text{m}$. A vertical grout pipe with a radius of $R = 10\,\text{mm}$ is inserted into the soil. Its bottom orifice is precisely located at the center of the domain $(0, 0, 0)$. To strictly adhere to the computational assumptions of porous media, the internal region of the grout pipe is excluded from the flow field calculations.

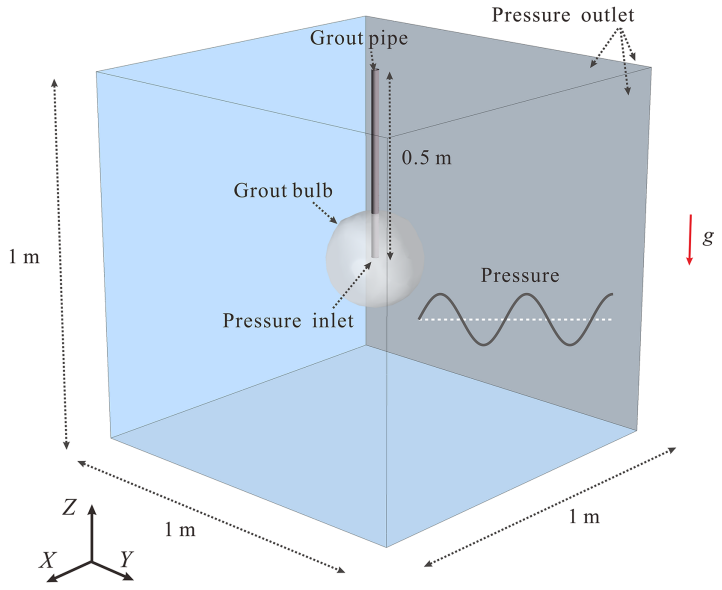


Figure 1: 3-D physical model and boundary conditions of the pulsating grouting in porous media.

A sinusoidal pulsating dynamic injection is applied at the bottom orifice. The transient inlet pressure boundary condition is mathematically defined as follows [2]:

$$P_{inlet} = P_{mean} + P_{amp} \sin\left(2\pi \cdot freq \cdot t\right) \tag{1}$$

where $P_{mean} = 1$ MPa is the mean injection pressure, $P_{amp} = 0.8$ MPa is the pressure amplitude, and $freq = 10$ Hz is the pulsating frequency. Concurrently, the top and side boundaries of the cubic domain are set as free pressure outlets, giving a relative pressure of $P_{outlet} = 0$ MPa.

The fluid domain employs the Volume of Fluid (VOF) method to track the gas-liquid two-phase interface [5]. The flow is assumed to be laminar. The density of the injected grout is set to $\rho_g = 1300\,\mathrm{kg/m^3}$, and its dynamic viscosity is $\mu_g = 0.028\,\mathrm{Pa \cdot s}$. The resident air in the pores adopts standard room temperature properties, with a density of $\rho_a = 1.225\,\mathrm{kg/m^3}$ and a dynamic viscosity of $\mu_a = 1.789 \times 10^{-5}\,\mathrm{Pa \cdot s}$. Gravity $\mathbf{g}$ acts along the negative Z-axis.

The porous medium is characterized by a uniform particle diameter $d_p = 1\,\mathrm{mm}$ and a porosity $\phi = 0.45$. According to the Kozeny-Carman equation, which has been widely validated in recent porous media studies [31–33], the absolute permeability K_{perm} of the matrix is calculated as:

$$K_{perm} = \frac{d_p^2 \phi^3}{180\left(1-\phi\right)^2} \approx 1.67 \times 10^{-9}\,\mathrm{m^2} \tag{2}$$

To simulate the flow resistance effect of the porous media in the CFD solver, a momentum source term based on Darcy's law must be introduced [34]. Therefore, the corresponding viscous resistance coefficient D is calculated as:

$$D = \frac{1}{K_{perm}} \approx 5.97 \times 10^{8}\,\mathrm{m^{-2}} \tag{3}$$

Under the VOF multiphase flow framework, the mixture density ρ_{mix} and mixture viscosity μ_{mix} within a grid cell are determined by the linear interpolation of the grout volume fraction $\alpha \in [0,1]$:

$$\rho_{mix} = \alpha\rho_g + \left(1-\alpha\right)\rho_a \tag{4}$$

$$\mu_{mix} = \alpha\mu_g + \left(1-\alpha\right)\mu_a \tag{5}$$

Given the extremely low flow velocity within the porous media, inertial forces can be neglected. Thus, this study adopts the macroscopic Darcy's Law to describe the flow kinematics. The apparent seepage velocity field $\mathbf{u}$ inside the porous media can be analytically expressed by the pressure gradient [35]:

$$\mathbf{u} = -\frac{K_{perm}}{\mu_{mix}}\left(\nabla P + \rho_{mix}\mathbf{g}\right) \tag{6}$$

Finally, the governing equations describing this two-phase displacement process consist of the continuity equation for incompressible fluids and the advection equation for the VOF phase interface:

$$\nabla \cdot \mathbf{u} = 0 \tag{7}$$

$$\frac{\partial \alpha}{\partial t} + \mathbf{u} \cdot \nabla \alpha = 0 \tag{8}$$

In the subsequent physics-informed neural network (PINN) surrogate model, the aforementioned velocity field **u** serves as a critical intermediate variable. It is explicitly calculated via the Automatic Differentiation (AD) engine and substituted into the continuity and VOF equations. This formulation constitutes the core physical soft constraints (Physics Loss) for the network optimization process [11].

2.2 Ground Truth Generation and Hybrid Sampling Strategy

To provide a clear macroscopic perspective of the proposed research framework, Fig. 2 illustrates the overall workflow. The process begins with high-fidelity CFD simulations to generate the transient multiphase flow data. Subsequently, a hybrid sampling strategy (70% spatial and 30% temporal) is applied to extract the training dataset. This dataset is then fed into the proposed cascaded FFM-PINN for optimization. Ultimately, the fully trained surrogate model achieves sub-second inference, serving as an efficient computational engine for structural digital twins.

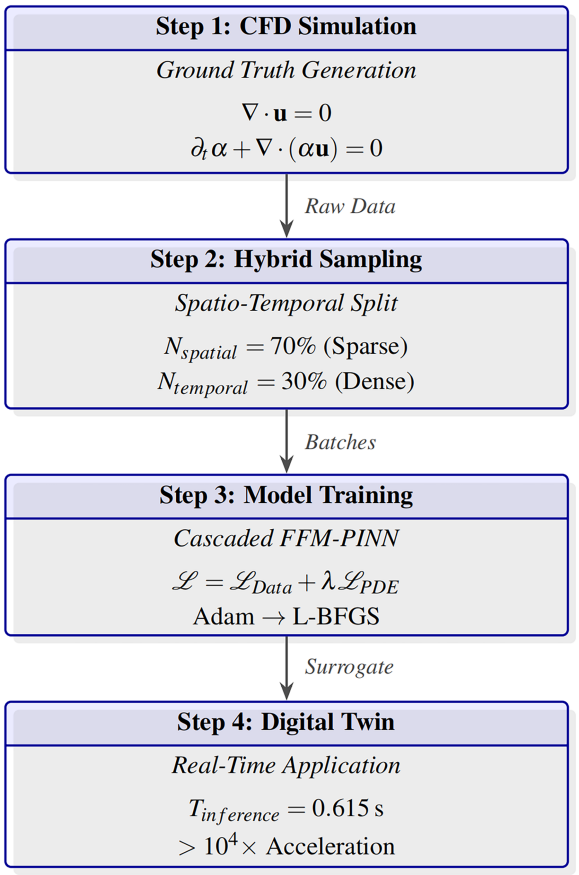


Figure 2: The overall workflow of the proposed physics-guided surrogate modeling framework.

To acquire high-fidelity datasets for the PINN surrogate model [6], a 3-D transient numerical simulation was conducted using ANSYS Fluent for a total duration of 2.0 s. A pressure-based transient solver was employed alongside the VOF multiphase model under laminar flow assumptions. Porous media flow resis-

tance was modeled by incorporating an implicit Darcy-based body force source term into the momentum equations. The Pressure Implicit with Splitting of Operators (PISO) algorithm handled the pressure-velocity coupling, while spatial discretization utilized the PREssure STaggering Option (PRESTO!) scheme for pressure and the second-order upwind scheme for momentum [36].

As depicted in Fig. 3a, the computational domain was discretized using a polyhedral mesh with local refinement near the injection pipe. The mesh comprises 444,556 cells with a minimum orthogonal quality of 0.203. To satisfy the stringent Courant-Friedrichs-Lewy (CFL) stability condition under the 10 Hz pulsation, the time step was strictly fixed at $\Delta t = 0.002$ s.

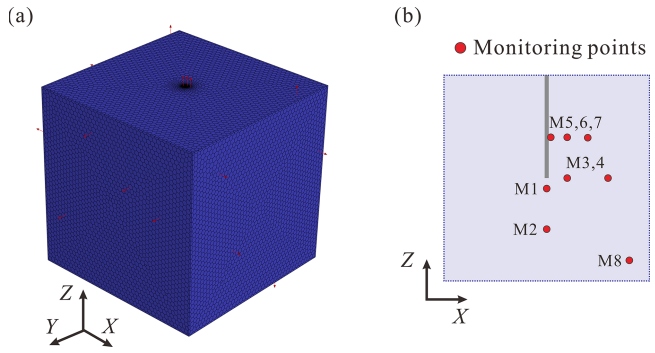


Figure 3: (**a**) Polyhedral mesh generation of the 3-D computational domain; (**b**) Layout of the monitoring points (M1~M8) on the *ZX* symmetry plane.

Although simulated in 3-D, the macroscopic grout diffusion is primarily dominated by radial and vertical dynamics. Because the gravity vector perfectly aligns with the vertical axis of the injection pipe (*Z*-axis), the flow field exhibits strict axisymmetry (cylindrical symmetry). While gravity causes a slight downward shift in the diffusion profile, this coaxial alignment ensures that any vertical plane passing through the central axis captures the identical physical evolution, fully preserving gravitational effects. Therefore, the *ZX* symmetry plane ($Y = 0$) passing through the grout pipe axis was extracted as the two-dimensional (2-D) training domain without any loss of physical fidelity. To simultaneously capture macroscopic spatial diffusion and microscopic high-frequency pulsations, a hybrid spatio-temporal sampling strategy is proposed:

(a) Macroscopic sparse spatial planar data: Full-field nodal state variables (x, z, t, P, α) on the *ZX* plane are extracted. To minimize data redundancy, the temporal sampling interval for this dataset is set to a relatively coarse $\Delta t = 0.2$ s.

(b) Microscopic high-frequency temporal monitoring point data: As shown in Fig. 3b, eight characteristic monitoring points (M1–M8) are deployed on the *ZX* plane. These points extract high-frequency time-series response data with a dense sampling interval consistent with the CFD time step ($\Delta t = 0.002$ s).

During the data loading phase of model training, the input data for each batch is strictly constrained to a mixing ratio of 70% spatial planar data and 30% temporal monitoring point data. This strategy effectively circumvents the risk of network overfitting in any single spatio-temporal dimension [37], thereby establishing a robust data foundation for accurately capturing high-frequency flow features.

2.3 Proposed Physics-Guided Cascaded PINN Framework

To address the formidable mathematical challenges posed by high-frequency dynamic boundaries and sharp multiphase flow interfaces, this study proposes a novel physics-guided cascaded neural network (designated as the state-of-the-art (SOTA) model). As illustrated in Fig. 4, the architecture deeply integrates physical causality with multiphase flow dynamics, consisting of three core modules:

(1) Module 1: Spatio-Temporal Feature Embedding

Traditional smooth activation functions suffer from severe "spectral bias," making them inadequate for fitting high-frequency signals [38,39]. To overcome this, Module 1 introduces Fourier Feature Mapping (FFM) [27,28]. The spatial coordinates (x, z) are mapped into high-frequency sine and cosine features $\mathbf{h}_{sp} = [\sin(\mathbf{Bx}), \cos(\mathbf{Bx})]$. Concurrently, to address the 10 Hz dynamic boundary, an explicit high-frequency encoding maps the time t into $\mathbf{h}_t = [\sin(2\pi f t), \cos(2\pi f t)]$ [40]. This decoupled feature embedding significantly enhances the network's perception of spatial mutations and temporal high-frequency pulsations.

(2) Module 2: Physics-Guided Cascaded Networks

This module adheres to the underlying physical logic that "phase state determines physical properties, and properties dictate the flow field." First, the VOF network prioritizes predicting the grout volume fraction. A Sigmoid activation function is applied as a hard constraint, mathematically eliminating non-physical out-of-bounds predictions (strictly ensuring $\alpha \in [0, 1]$) [41,42].

Subsequently, the predicted α enters the Physical Property Modulator, which calculates the local mixture density ρ_{mix} and viscosity μ_{mix} in real-time via linear interpolation. Finally, the state variables $(\alpha, \rho_{mix}, \mu_{mix})$ are concatenated as a strong physical prior into the hidden layers of the pressure network. This cascaded mechanism effectively decouples the strong multi-field nonlinearities and significantly improves convergence stability [15,35].

(3) Module 3: Gradient Regularization & Hybrid Loss

In complex multiphase flows, directly employing the full fluid dynamics equations as the loss function frequently triggers gradient pathologies [23,24]. Therefore, the Automatic Differentiation (AD) engine in Module 3 only extracts critical physical gradients $(\nabla P, \nabla\alpha, \partial_t\alpha)$ to construct a highly streamlined Gradient Regularization term as the physics loss $\mathcal{L}_{PDE}$. For the data loss $\mathcal{L}_{Data}$, the model utilizes the aforementioned hybrid sampling dataset and applies a 10× weight penalty to the VOF error to accelerate the sharpening and fitting of the gas-liquid interface.

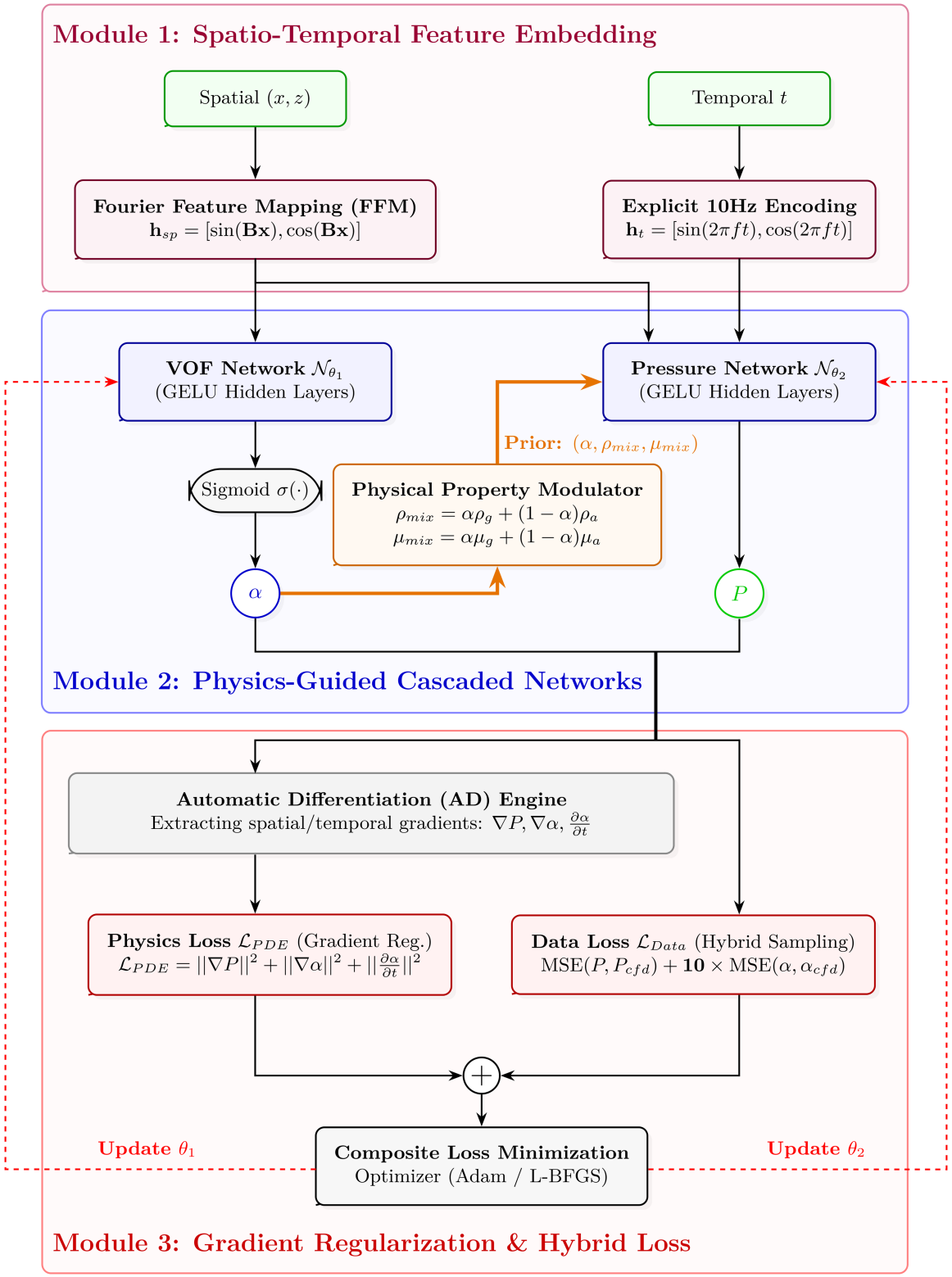


Figure 4: Schematic diagram of the proposed cascaded PINN framework, detailing the spatio-temporal feature embedding (Module 1), physics-guided cascaded networks (Module 2), and gradient regularization with hybrid loss (Module 3).

2.4 Evolution of PINN Architectures and Ablation Design

To systematically disentangle and verify the independent contributions of network topologies, high-frequency activation mechanisms, and loss function reformulations to the multiphase flow resolution accuracy, a rigorous ablation study was designed. Rooted in the underlying theory of Physics-Informed Neural Networks (PINNs), three progressively evolved surrogate architectures were constructed.

(1) Model 1: Baseline PINN

As illustrated in Fig. 5, Model 1 employs a traditional parallel dual-branch Multi-Layer Perceptron (MLP) structure, independently predicting the volume fraction (VOF) and pressure fields. From the perspective of Neural Tangent Kernel (NTK) theory, MLPs equipped with conventional smooth activation functions (e.g., Swish or Tanh) suffer from severe "spectral bias," meaning the network inherently prioritizes fitting the low-frequency components of the target function [43]. Although explicit temporal high-frequency features are concatenated at the input, the network still acts as a low-pass filter, failing to acutely capture the 10 Hz severe pressure pulsations. Furthermore, Model 1 utilizes a soft penalty to constrain the VOF boundaries. In highly nonlinear multiphase flows, soft penalties frequently fail, outputting non-physical values ($\alpha < 0$ or $\alpha > 1$). This not only violates mass conservation but also directly triggers a breakdown in subsequent mixture density and viscosity calculations.

(2) Model 2: Cascaded SIREN Surrogate

To eliminate the physical causality deficits in Model 1, Model 2 (Fig. 6) introduces a Cascaded Dual-Branch Architecture. This architecture hardcodes the physical causality (i.e., "phase state determines physical properties, which in turn dictate the flow field") directly into the forward pass as a physical inductive bias. The predicted α, after being strictly projected into the $[0, 1]$ space via a Sigmoid hard constraint, is fed as a hard prior into the pressure network. Crucially, this sequence guarantees physical boundedness during the forward pass. The network first outputs an unbounded latent variable, which is immediately projected into the [0, 1] range via the Sigmoid layer. When the automatic differentiation engine computes the gradients for the physics loss, it operates exclusively on these already-bounded values, mathematically eliminating the possibility of non-physical states prior to PDE evaluation.

At the feature activation level, Model 2 adopts Sinusoidal Representation Networks (SIREN, $\omega_0 = 30$). Because the higher-order derivatives of a sine function remain sinusoidal, SIREN significantly alters the NTK spectral distribution. When processing raw spatio-temporal coordinates $\mathbf{X} = (x, z, t)$, it possesses an exceptionally strong capability to perceive and reconstruct sharp spatial gradients (gas-liquid interfaces) and high-frequency temporal transients (pulsating pressures). For the SIREN activation, a systematic empirical search ($\omega_0 = 10, 20, 30, 40, 50$) was conducted prior to finalization. Lower values ($\omega_0 \leq 20$) reverted to spectral bias, failing to capture the 10 Hz pulsations, while higher values ($\omega_0 \geq 40$) rendered the loss landscape excessively rugged, triggering severe numerical noise. Therefore, $\omega_0 = 30$ was selected as it provided the optimal balance between high-frequency perception and training stability.

(3) Model 3: Proposed SOTA Model (Cascaded PINN with FFM)

Although SIREN excels in high-frequency reconstruction, its highly oscillatory activation landscape makes deep networks prone to falling into local minima when confronted with complex fluid dynamics equations, leading to training instability [22]. Therefore, the final proposed SOTA model (Model 3, topology detailed in Fig. 7) retains the physical cascaded logic and hard constraint mechanisms of Model 2 but reformulates the feature mapping.

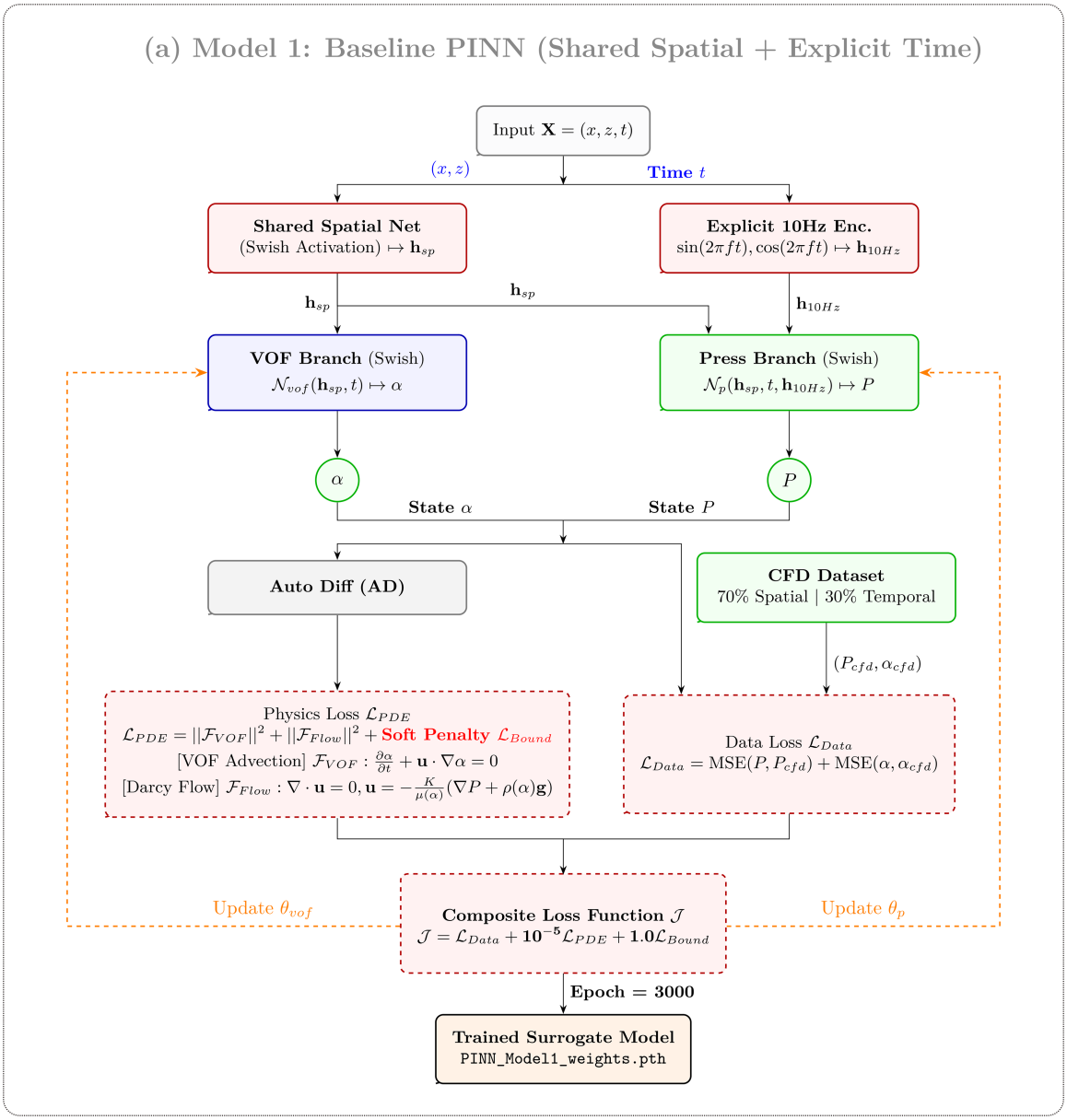


Figure 5: Schematic of Model 1: The baseline PINN architecture featuring parallel branches, Swish activation, soft boundary constraints, and full partial differential equation (PDE) loss.

Model 3 employs a combination of Fourier Feature Mapping (FFM) + explicit temporal encoding + GELU activation. FFM projects low-dimensional spatial coordinates into a high-frequency Fourier space via a non-trainable random matrix **B**, fundamentally overcoming spectral bias [44,45]. Meanwhile, the GELU activation ensures the smoothness of the loss landscape and optimization stability [46]. This decoupled strategy achieves an optimal balance between "high-frequency fitting capability" and "global convergence robustness."

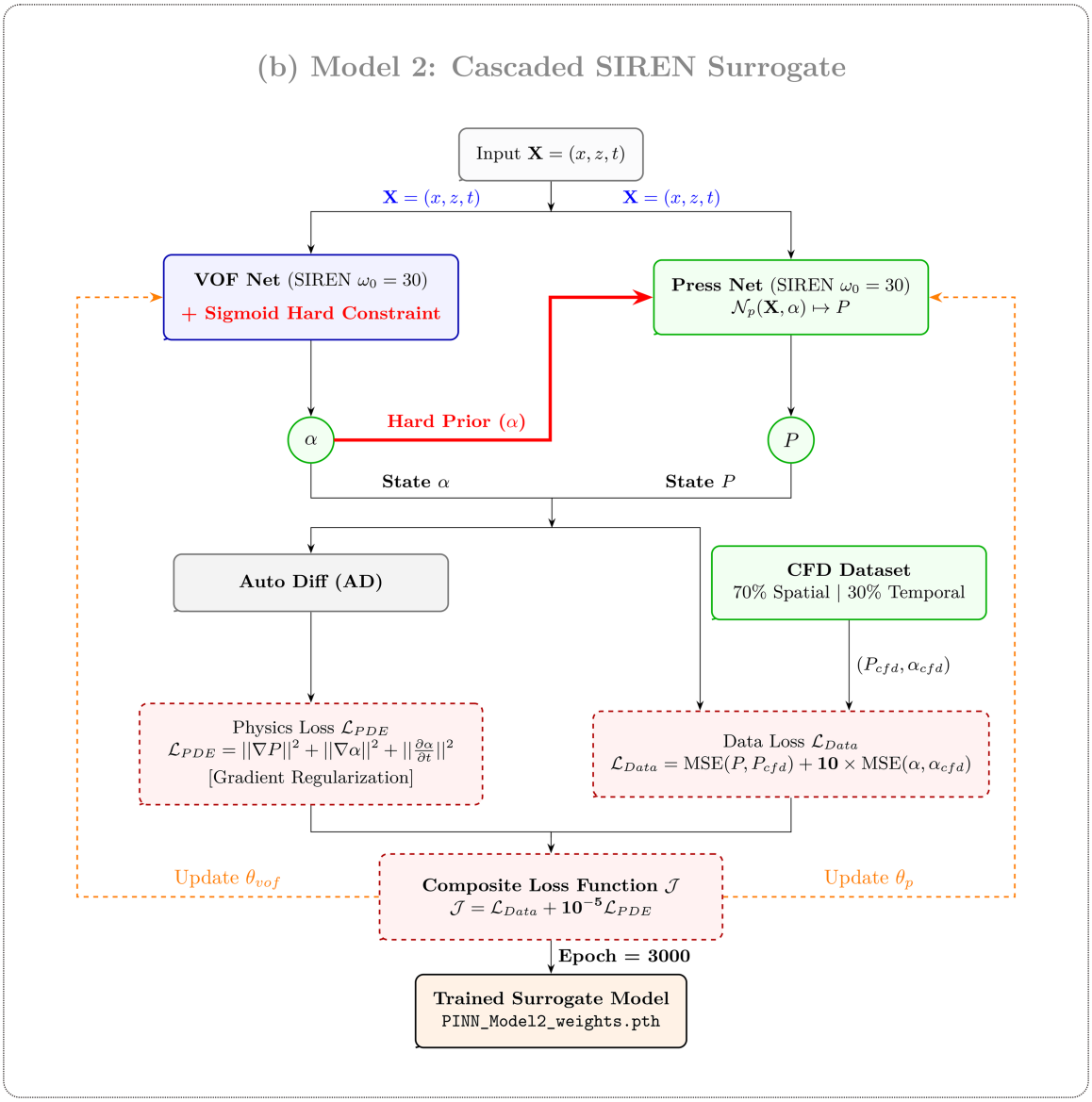


Figure 6: Schematic of Model 2: The cascaded surrogate architecture utilizing the SIREN activation function, Sigmoid hard constraints, and gradient regularization mechanisms.

2.5 Composite Loss Function

During the PINN optimization process, the composite loss function $\mathcal{J}$ for all three models is formulated by weighting the data loss ($\mathcal{L}_{Data}$) and the physics loss ($\mathcal{L}_{PDE}$).

Rooted in the principle of Empirical Risk Minimization (ERM), the Data Loss ($\mathcal{L}_{Data}$) quantifies the Mean Squared Error (MSE) between the network predictions and the hybrid sampled CFD dataset. To accelerate the convergence of the high-gradient gas-liquid interface, a 10× penalty weight is applied to the VOF error:

$$\mathcal{L}_{Data} = \text{MSE}\left(P, P_{cfd}\right) + 10 \times \text{MSE}\left(\alpha, \alpha_{cfd}\right) \tag{9}$$

where P is the predicted pressure field (Pa); P_{cfd} is the ground truth pressure provided by the CFD dataset (Pa); α is the predicted grout volume fraction (dimensionless); and α_{cfd} is the ground truth volume fraction from the CFD dataset (dimensionless).

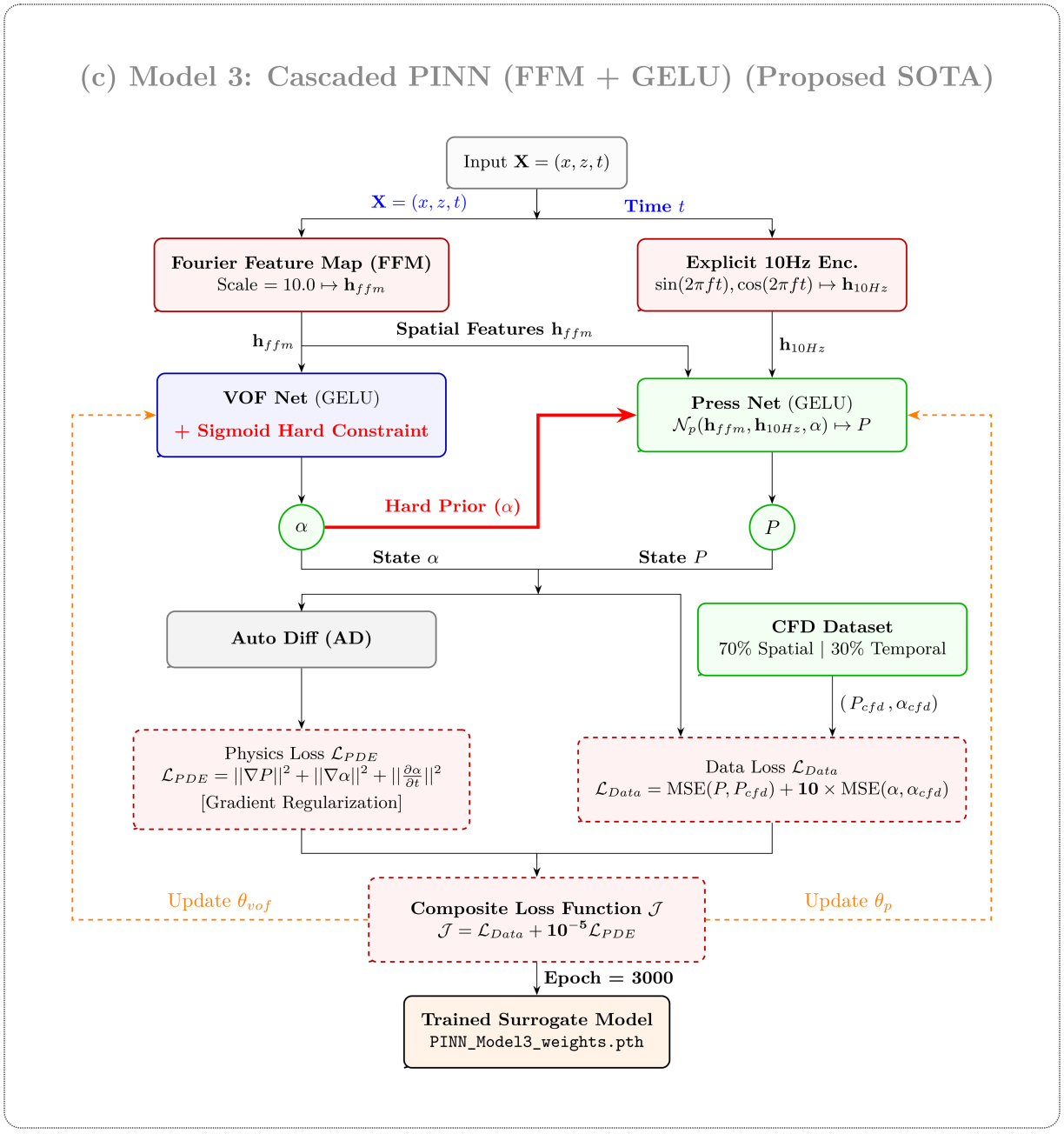


Figure 7: Schematic of Model 3: The proposed SOTA model, integrating Fourier Feature Mapping (FFM), physical cascaded logic, and hybrid loss mechanisms.

The formulation of the Physics Loss ($\mathcal{L}_{PDE}$) fundamentally differs across the models, directly dictating the optimization difficulty:

For Model 1, the physics loss consists of the full VOF advection equation residual, the Darcy flow equation residual, and a VOF soft boundary penalty. Due to the massive magnitude disparities among different partial differential terms, this full-equation constraint frequently triggers gradient pathologies, causing severe conflicts in the gradient directions during backpropagation [47–49].

$$\mathcal{L}_{PDE}^{\text{Model1}} = ||\mathcal{F}_{VOF}||^2 + ||\mathcal{F}_{Flow}||^2 + \mathcal{L}_{Bound} \tag{10}$$

where $\mathcal{F}_{VOF}$ represents the partial differential residual of the VOF advection equation (s^{-1}); $\mathcal{F}_{Flow}$ denotes the partial differential residual of the incompressible Darcy flow equation (s^{-1}); and $\mathcal{L}_{Bound}$ is the soft boundary penalty term designed to restrict the volume fraction within physical limits (dimensionless).

For Model 2 and Model 3, since the cascaded architecture and hard constraints have already injected substantial physical information as an "inductive bias," imposing full-equation constraints would render the model over-constrained. Therefore, their physics loss is drastically streamlined into pure Gradient Regularization. Analogous to Sobolev Training, this mechanism extracts only critical first-order spatio-temporal gradients via automatic differentiation [50]. While avoiding gradient conflicts, it effectively suppresses non-physical spurious oscillations that may arise during high-frequency fitting, ensuring the smoothness of the flow field reconstruction:

$$\mathcal{L}_{PDE}^{\text{Model2,3}} = ||\nabla P||^2 + ||\nabla \alpha||^2 + \left|\left|\frac{\partial \alpha}{\partial t}\right|\right|^2 \tag{11}$$

where ∇P is the spatial gradient of the pressure field ($Pa \cdot m^{-1}$); $\nabla \alpha$ is the spatial gradient of the volume fraction (m^{-1}); and $\frac{\partial \alpha}{\partial t}$ is the first-order partial derivative of the volume fraction with respect to time (s^{-1}).

Ultimately, the network minimizes the total objective function via Adam or Limited-memory Broyden-Fletcher-Goldfarb-Shanno (L-BFGS) optimizers until full convergence is achieved [12]:

$$\mathcal{J} = \mathcal{L}_{Data} + \lambda \mathcal{L}_{PDE} \tag{12}$$

where $\mathcal{J}$ is the total objective function for network optimization (dimensionless); and λ is the adaptive weight coefficient balancing the data loss and physics loss (dimensionless).

2.6 Hyperparameter Configuration and Hardware Environment

To ensure the reproducibility of the proposed surrogate models, the detailed hyperparameter configurations, optimizer strategies, and the hardware environment utilized during the network training process are summarized in Table 1.

Table 1: Hyperparameter configurations and hardware specifications for the proposed model.

Category	Parameter/Component	Specification
Network Architecture	Hidden Layers	6
	Neurons per Layer	128
	Activation Function	GELU (Model 3)/SIREN (Model 2)
	Initialization Strategy	Xavier Normal

(Continued)

Table 1 (continued)

Category	Parameter/Component	Specification
Training Strategy	Initial Learning Rate	1×10^{-3} (with exponential decay)
	Optimizer (Phase 1)	Adam (0–2000 epochs)
	Optimizer (Phase 2)	L-BFGS (2000 epochs to convergence)
	Loss Weight (λ_{vof})	10
Computational Setup	Hardware graphics processing unit (GPU)	Single NVIDIA GPU (48 GB Video Random Access Memory)
	Hardware (CPU & RAM)	Intel Xeon Platinum 8470Q (92 GB RAM)
	Deep Learning Framework	PyTorch 2.1.2 (Python 3.10, CUDA 11.8)

3 Results of Multiphase Flow Reconstruction

Based on the theoretical framework and hybrid spatio-temporal sampling strategy established in Chapter 2, this section systematically evaluates the solution accuracy of the proposed PINN surrogate models. To isolate and verify the independent contributions of network topologies and activation functions to the resolution of high-frequency pulsating multiphase flows, a rigorous ablation study is designed, comparing three progressively evolved architectures: Model 1 (Baseline PINN), Model 2 (Cascaded SIREN Surrogate), and Model 3 (Proposed SOTA Model).

3.1 Spatial Reconstruction of Macroscopic Flow Fields

Using the high-fidelity numerical results from the Computational Fluid Dynamics (CFD) solver as the ground truth, this section first evaluates the capability of the three architectures to reconstruct macroscopic spatio-temporal evolution features. Fig. 8 illustrates the cross-sectional contours of the volume fraction (VOF) at $t = 2$ s. It is observed that Model 1 fails to accurately capture the multiphase boundary and morphological features (Fig. 8b), exhibiting significant numerical dissipation. The error distribution (Fig. 8e) indicates that the local relative error near the grout diffusion boundary approaches 40%. While Model 2 maintains relatively low errors near the injection outlet, it suffers from severe divergence around the grout bubble, particularly at the peripheral interfaces where the maximum error peaks at 80% (Fig. 8f,h). Furthermore, the far-field region is plagued by widespread non-physical oscillations with errors reaching 40%, rendering Model 2 entirely unsuitable for identifying the grout diffusion range. In stark contrast, Model 3 achieves exceptional precision across the entire computational domain. Even at the highly nonlinear grout diffusion boundaries, the local error is strictly constrained below 10% (Fig. 8g), demonstrating its superior capability in high-fidelity macroscopic flow field reconstruction.

The pressure field distributions at $t = 2$ s in Fig. 9 further reveal the limitations of the baseline models in spatial reconstruction. The CFD ground truth in Fig. 9a displays a natural circular high-pressure bubble that conforms to physical diffusion laws. Model 1 severely distorts this morphological feature by producing a flattened pressure bubble and overestimating the peak pressure, leading to a localized relative error of up to 25% (Fig. 9b,e). Furthermore, Model 2 completely fails to capture the core pressure bubble while introducing chaotic, non-physical fluctuations across the mid-to-far field (Fig. 9c,f). Conversely, Model 3 accurately reconstructs the circular pressure bubble and maintains a highly stable far-field distribution with peak values closely matching the CFD results (Fig. 9d). The zoomed-in error analysis near the injection pipe in Fig. 9h clearly quantifies this performance gap. Model 3 strictly constrains the maximum relative error to approximately 5%, demonstrating a significant improvement over the 15% error observed in Model 2 and the 25% error in Model 1.

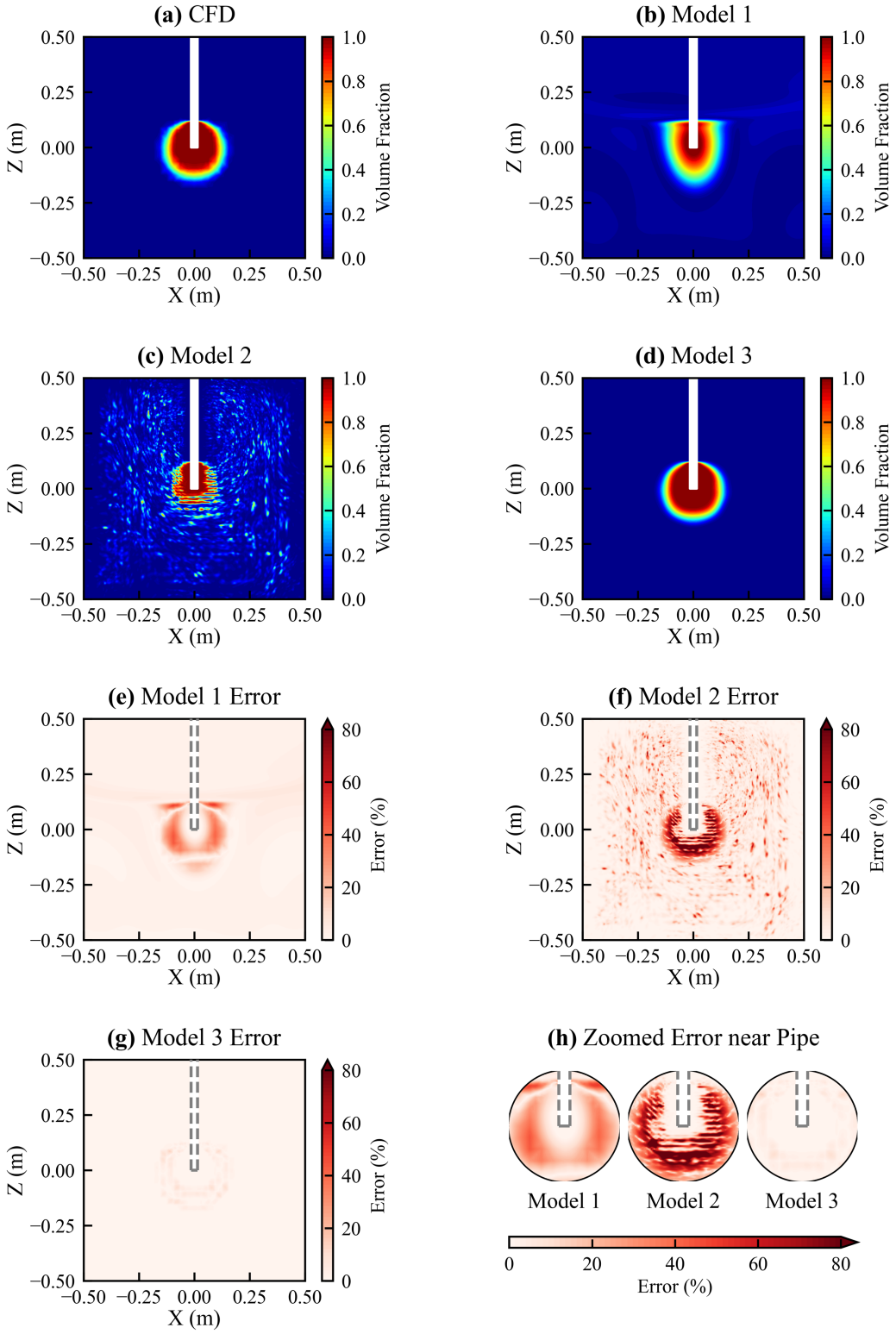


Figure 8: Cross-sectional contours of the volume fraction (VOF) and local error comparison at t = 2 s. (**a**) CFD ground truth; (**b**) Model 1 prediction; (**c**) Model 2 prediction; (**d**) Model 3 prediction; (**e**–**g**) Corresponding relative error distributions; (**h**) Zoomed-in error near the injection pipe.

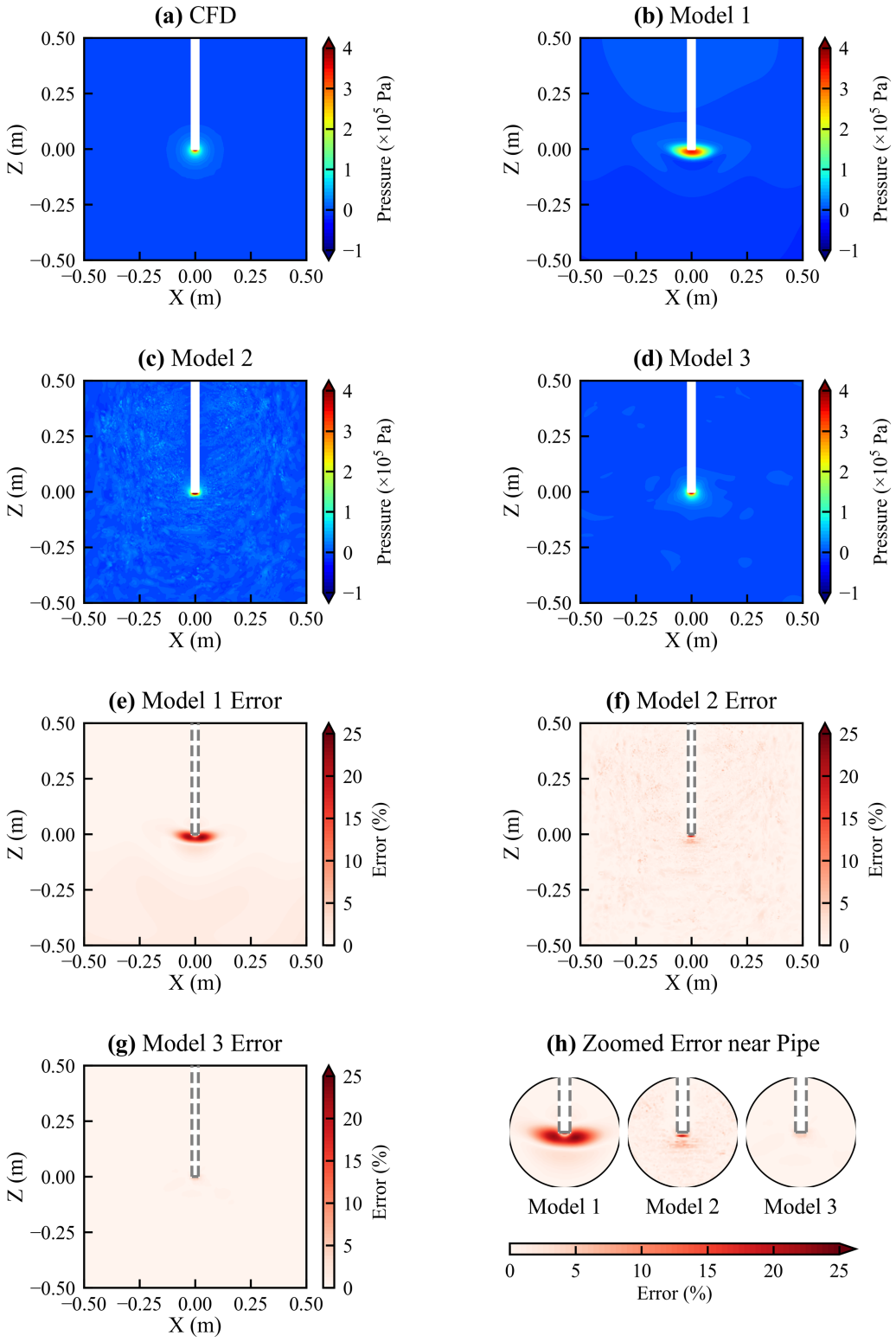


Figure 9: Cross-sectional contours of the pressure field and local error comparison at $t = 2$ s. (**a**) CFD ground truth; (**b**) Model 1 prediction; (**c**) Model 2 prediction; (**d**) Model 3 prediction; (**e**–**g**) Corresponding relative error distributions; (**h**) Zoomed-in error near the injection pipe.

3.2 Transient Tracking of High-Frequency Dynamic Boundaries

To evaluate the temporal stability of the predictive models, Fig. 10 presents the pressure time-history curves and corresponding absolute errors at four characteristic monitoring points. Model 1 exhibits severe numerical divergence across all locations. At the near-field point M1, it completely fails to track the 10 Hz high-frequency pulsation, while simultaneously suffering from massive negative baseline drifts in the mid-to-far field regions at M3, M6, and M8. Although Model 2 captures the macroscopic trend of the near-field pulsation, it introduces severe spurious high-frequency oscillations away from the injection source. This instability prevents Model 2 from maintaining the physically stable zero-pressure state in the far field, resulting in continuous and chaotic error fluctuations. Conversely, Model 3 demonstrates exceptional temporal robustness. It accurately resolves the highly dynamic transient fluctuations at M1 and strictly suppresses non-physical noise in the far field, thereby maintaining near-zero absolute errors throughout the entire simulation period.

Following the validation of spatial flow field reconstruction, this section evaluates the surrogate models' temporal tracking accuracy regarding the transient evolution of the multiphase flow interface. As established in the previous section, Model 1 is excluded from this analysis due to its severe numerical divergence, allowing a focused comparison between Model 2 and Model 3. Fig. 11 illustrates the time-history curves of the volume fraction (VOF) at characteristic monitoring points, supplemented by high-resolution zoomed-in views. Overall, Model 3 demonstrates exceptional phase alignment capabilities, whereas Model 2 suffers from severe numerical volatility.

At the near-field and mid-field locations M1 and M3, the VOF undergoes a highly nonlinear growth phase as the grout front arrives. During this critical transient stage, the prediction curve of Model 3 exhibits strong agreement with the CFD ground truth. Conversely, the zoomed-in intervals clearly reveal that Model 2 introduces continuous high-frequency fluctuation errors around the physical baseline, severely degrading the tracking precision of the phase interface. This numerical instability is most pronounced in the unaffected far-field regions M6 and M8. While the physical VOF must strictly remain at 0, Model 2 exhibits intense non-physical oscillations. In stark contrast, Model 3 maintains a highly stable zero baseline throughout the entire simulation. These results confirm that Model 2 fails to meet the rigorous stability requirements for multiphase flow modeling, whereas the proposed mechanisms in Model 3 ensure high-fidelity temporal tracking.

Fig. 12 evaluates the temporal response of the models to high-frequency pulsating pressures. At the near-field injection inlet (M1), both Model 2 and Model 3 accurately capture the pressure peaks and troughs, exhibiting comparable transient tracking capabilities that strongly agree with the CFD ground truth. However, significant discrepancies emerge as the flow propagates into the mid-to-far field (M3, M6, M8). In these regions, Model 2 is plagued by severe high-frequency interference, producing non-physical spurious oscillations up to 1×10^4 Pa. Conversely, Model 3 effectively suppresses this numerical noise, maintaining a highly stable baseline that closely matches the CFD predictions. Consequently, while Model 2 performs adequately in the near-field, Model 3 demonstrates comprehensive superiority by successfully overcoming numerical instability under high-frequency dynamic boundaries, ensuring a high-fidelity reconstruction of the global transient pressure field.

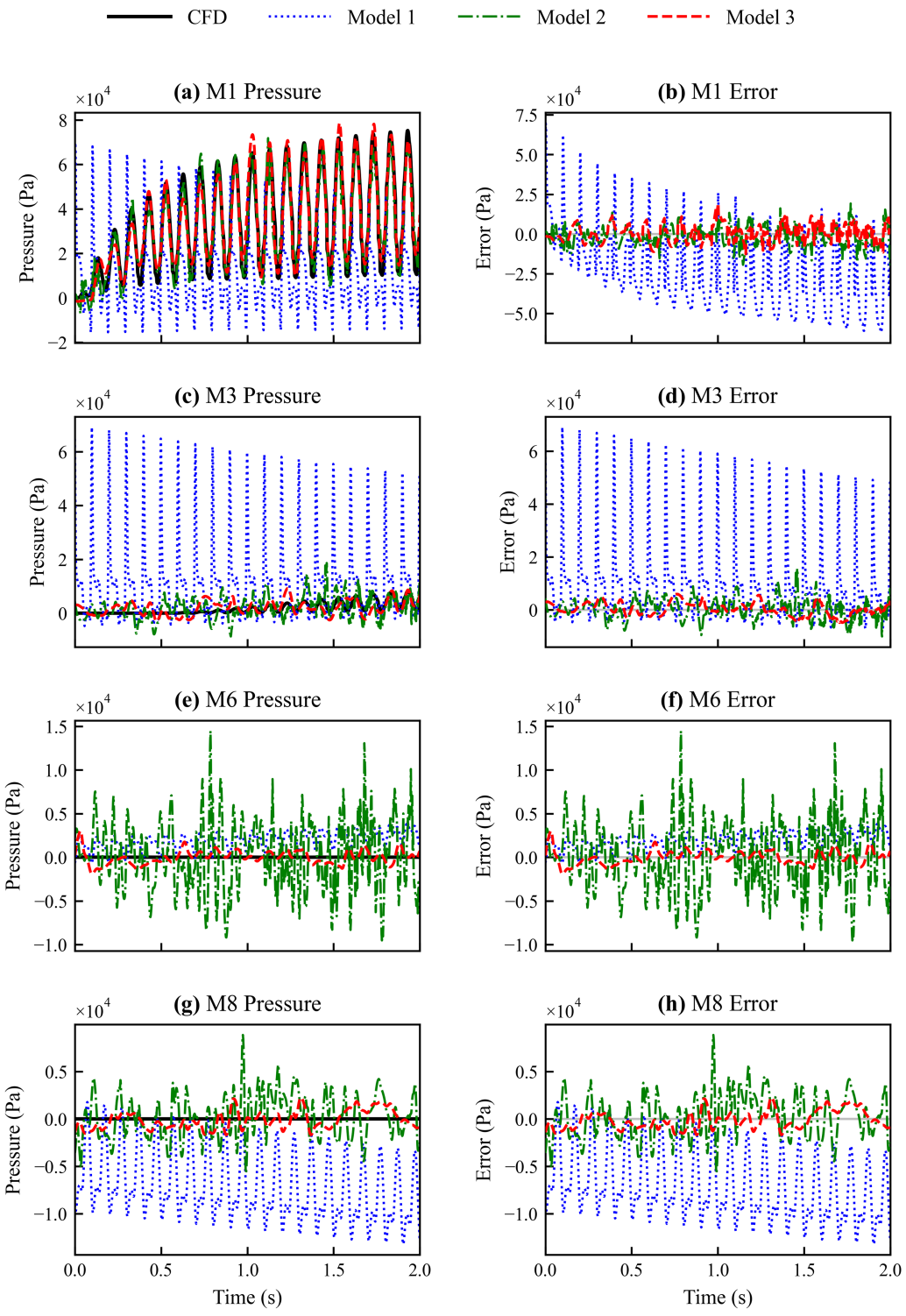


Figure 10: Time-history curves and corresponding absolute errors of the pressure field at local characteristic monitoring points M1, M3, M6, and M8.

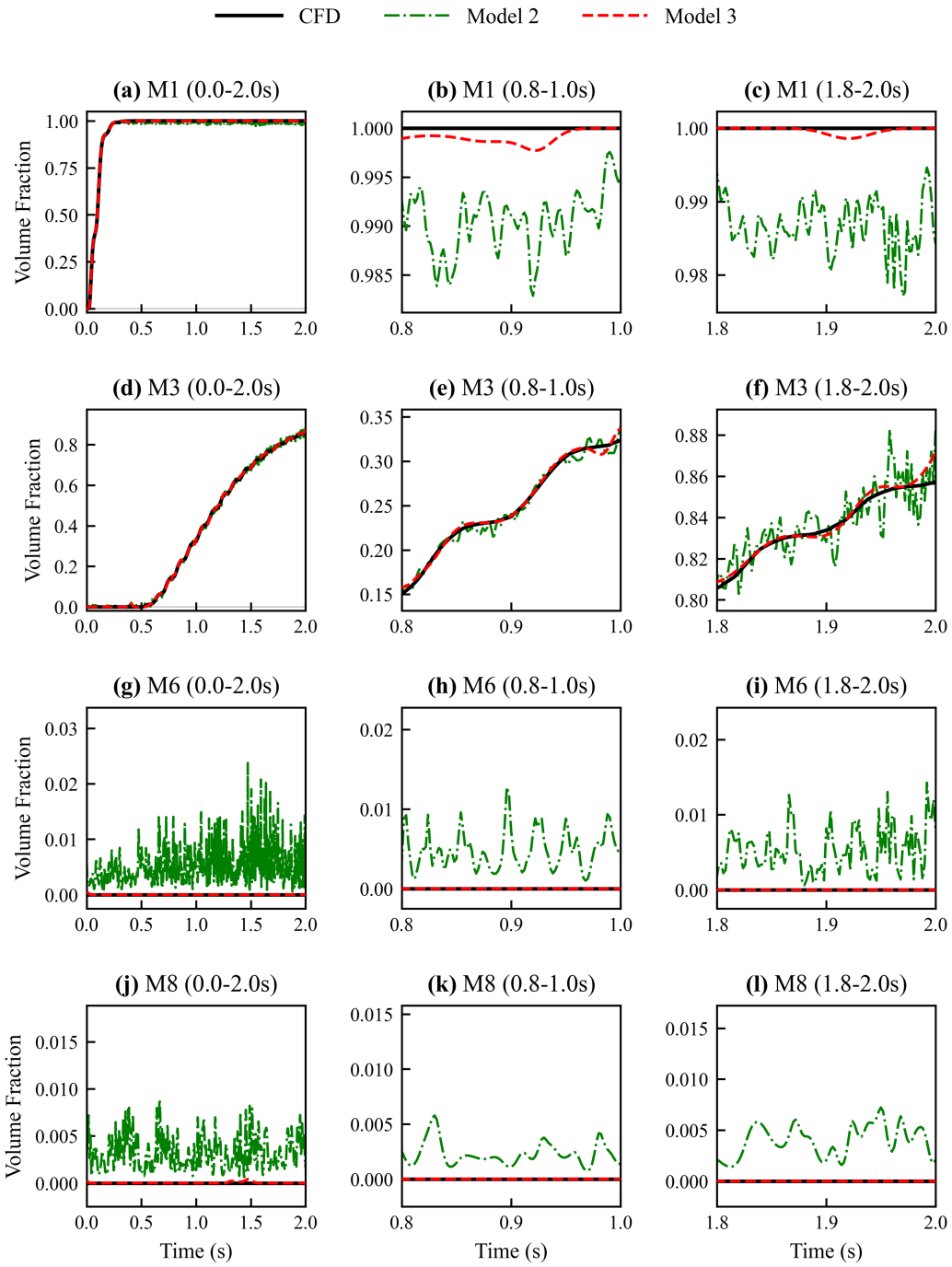


Figure 11: Time evolution of the volume fraction (VOF) at characteristic monitoring points M1, M3, M6, and M8. The left column presents the full simulation period, while the middle and right columns provide high-resolution zoomed-in views of specific transient intervals.

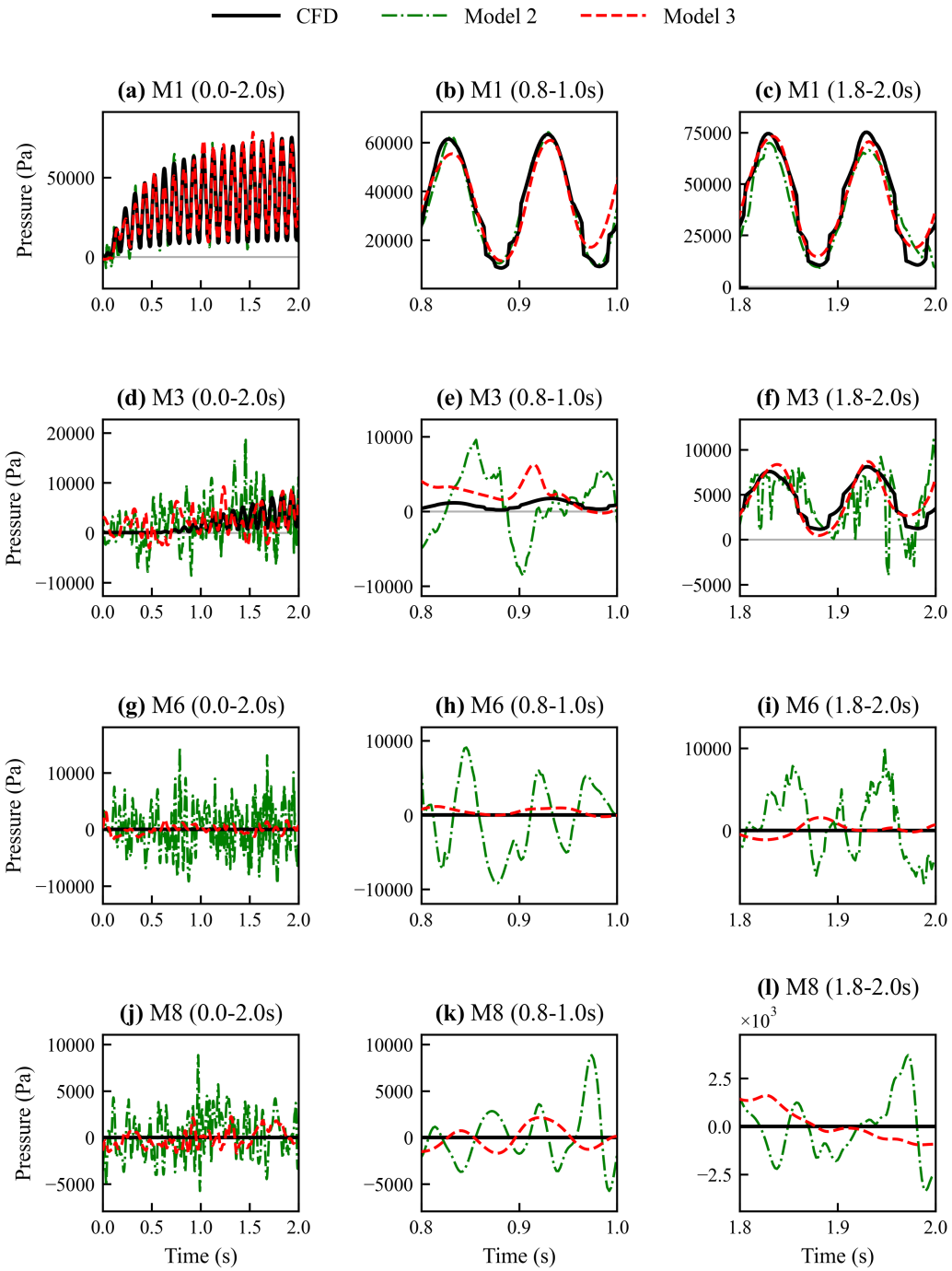


Figure 12: Transient pressure evolution at characteristic monitoring points. The left column presents the macroscopic response over the full 0.0–2.0 s period, while the middle and right columns detail the high-frequency pulsations within the 0.8–1.0 s and 1.8–2.0 s intervals, respectively.

3.3 Global Quantitative Evaluation and Computational Efficiency

To evaluate the global statistical robustness of the proposed framework, Fig. 13 compares the predicted volume fraction distributions against the CFD ground truth. High-fidelity predictions should theoretically align with the ideal $y = x$ diagonal. As depicted in Fig. 13a, Model 1 exhibits severe numerical divergence, with numerous points escaping the ±50% error bands across the domain. Most notably, it fails to accurately

resolve the critical phase interface defined at a volume fraction of 0.5, resulting in chaotic scattering and a fundamental inability to capture dynamic boundaries.

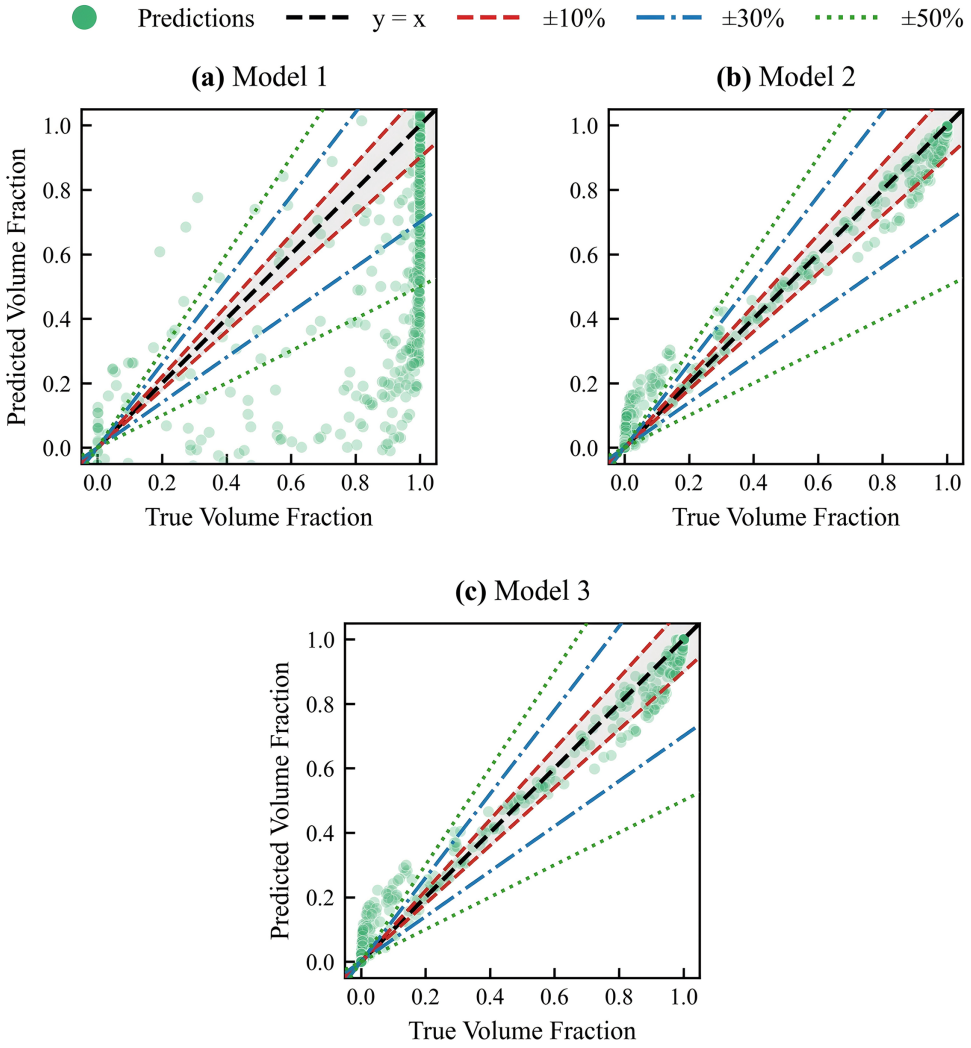


Figure 13: Global scatter distribution comparing the predicted volume fraction values against the CFD ground truth. (**a**) Model 1; (**b**) Model 2; (**c**) Model 3.

Conversely, Models 2 and 3 (Fig. 13b,c) demonstrate highly comparable and superior phase-tracking capabilities. Near the injection inlet where the volume fraction approaches 1.0, and at the phase interface of 0.5, both models strictly adhere to the diagonal, restricting the vast majority of predictions within a narrow ±10% error band. While both models exhibit apparent visual dispersion in the far-field where the true volume fraction approaches zero, this is primarily a mathematical artifact of relative error metrics. In these near-zero regions, minute absolute numerical fluctuations are significantly amplified. Overall, Models 2 and 3 show no significant statistical differences in global volume fraction prediction, as both successfully achieve high-fidelity phase reconstruction and overcome the catastrophic divergence of Model 1.

Fig. 14 presents the global scatter distribution comparing the predicted pressure values of the three architectures against the CFD ground truth. For Model 1, significant deviations are observed in the high-pressure zone near the injection port, where it systematically overestimates the pressure, with numerous points exceeding the +50% error band. Furthermore, in the mid-to-low pressure regions representing

the mid-to-far field, scatter points are widely dispersed, frequently escaping the ±50% boundaries. Model 2 improves upon this baseline; however, in the high-pressure zone, it tends to underestimate the peak pressure, with a distinct cluster of predictions falling outside the −10% error band and approaching the −30% boundary. Additionally, in the far-field where the true pressure approaches zero, Model 2 still exhibits noticeable numerical dispersion. In contrast, Model 3 demonstrates the highest accuracy. In the high-pressure injection vicinity, its deviations are minimal, with the vast majority of points tightly restricted within the ±10% error band. Similarly, in the far-field regions, the scattered points are highly concentrated along the $y = x$ diagonal. Overall, Model 3 achieves the most optimal global pressure reconstruction among the three algorithms.

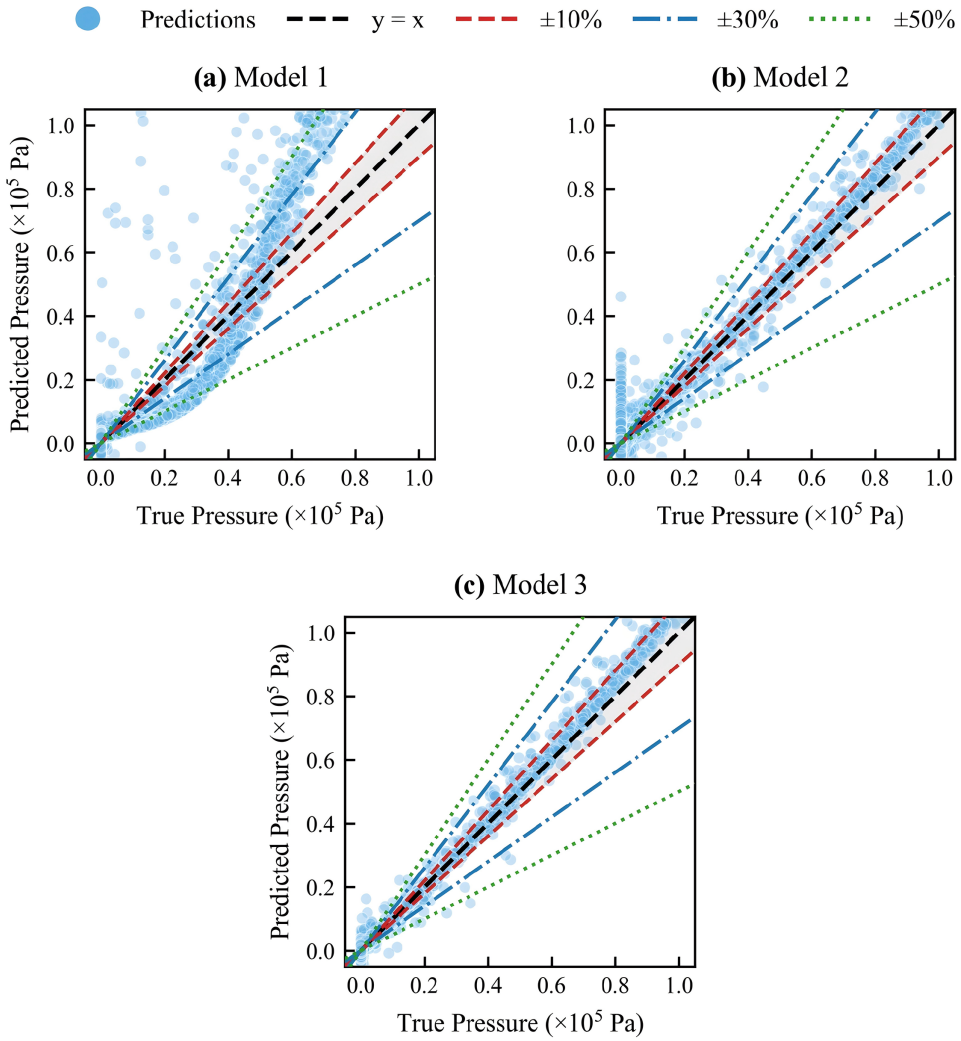


Figure 14: Global scatter distribution comparing the predicted pressure values with the CFD ground truth. (**a**) Model 1; (**b**) Model 2; (**c**) Model 3.

Fig. 15 presents a quantitative comparison of global errors and computational efficiency across the evaluated architectures. The preceding evaluations systematically demonstrate the superior performance of the proposed cascaded FFM-PINN architecture (Model 3) in simulating pulsating grouting multiphase flows [51–53]. By comparing the three architectures, clear performance boundaries and mechanistic differences are established.

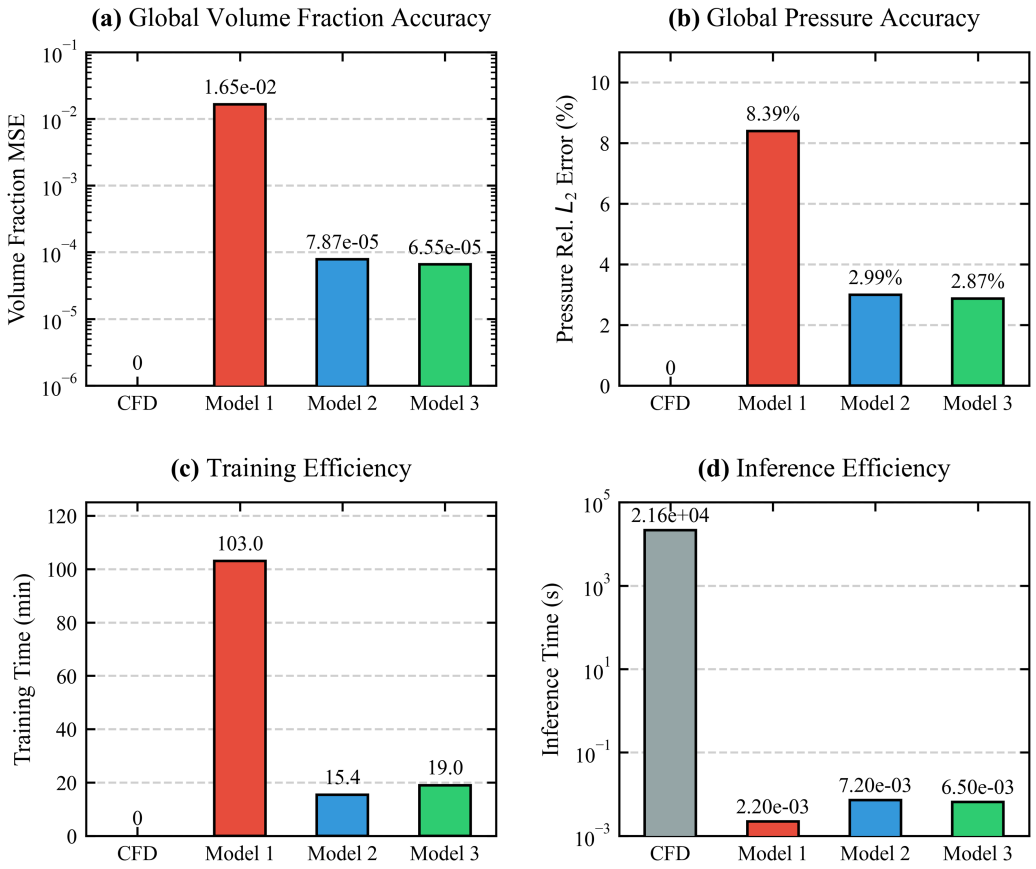


Figure 15: Quantitative comparison of global accuracy and computational efficiency among different architectures. (**a**) Global VOF accuracy; (**b**) Global pressure accuracy; (**c**) Training efficiency; (**d**) Inference efficiency.

Regarding physical field reconstruction (Fig. 15a,b), Model 1 (Baseline PINN) exhibits the lowest accuracy. Constrained by spectral bias and gradient conflicts, it suffers from severe numerical smearing at the phase interfaces and fails to capture the dynamic pressure bubbles, resulting in a high Volume of Fluid (VOF) Mean Squared Error (MSE) of 1.65×10^{-2} and a global pressure error of 8.39%. Model 2 (Cascaded SIREN) improves upon this by successfully capturing the high-frequency pressure fluctuations near the injection inlet. However, its purely periodic activation function introduces noticeable non-physical high-frequency oscillations in the mid-to-far field. This mathematical artifact severely degrades the identification of the phase interface and causes continuous chaotic fluctuations in the far-field pressure, yielding a VOF MSE of 7.87×10^{-5} and a pressure error of 2.99%.

In contrast, Model 3 achieves the most optimal balance. By synergizing Fourier Feature Mapping (FFM) with GELU activations, it accurately resolves both the sharp phase interfaces and the transient pressure bubbles. It tracks the 10 Hz pulsations perfectly in the near-field while maintaining strict numerical stability in the far-field, effectively eliminating the spurious oscillations observed in Model 2. Quantitatively, Model 3 achieves the best global metrics, reducing the VOF MSE to 6.55×10^{-5} and the pressure error to 2.87%.

Computationally (Fig. 15c,d), the proposed framework transitions from traditional numerical iteration to data-driven inference. Confronted with a 10 Hz forced boundary, traditional CFD solvers are strictly constrained by the Courant-Friedrichs-Lewy (CFL) condition, necessitating time-consuming implicit iterations that consume 2.16×10^4 s (6.0 h) per evolution. Conversely, the fully trained Model 3 executes only matrix multiplications and nonlinear mappings, compressing the inference time to 6.50×10^{-3} s for the exact 2D

axisymmetric equivalent field. While maintaining high global statistical fidelity, this model achieves a computational acceleration of over six orders of magnitude, providing an efficient millisecond-level underlying engine for digital twin systems of underground structures and foundation grouting processes [54,55].

4 Comprehensive Discussion and Model Robustness

While Section 3 established the superior predictive accuracy and computational efficiency of the proposed SOTA model, this section delves deeper into the underlying mechanisms driving these achievements. By analyzing the training dynamics, posterior physical consistency, and hyperparameter sensitivity, we comprehensively evaluate the robustness and engineering applicability of the surrogate framework.

4.1 Training Dynamics and Convergence Analysis

To elucidate the underlying convergence mechanisms and computational advantages of the proposed architecture, the real-time training dynamics of the three models are systematically compared. As illustrated in Fig. 16, Model 3 exhibits a remarkably accelerated and stable convergence trajectory. Fig. 16a demonstrates that while the Baseline MLP (Model 1) requires approximately 100 min to reach a suboptimal plateau, the Cascaded FFM-PINN (Model 3) achieves a significantly lower total loss in merely 19 min. This confirms that the acceleration is driven by the architectural resolution of spectral bias rather than hardware variations.

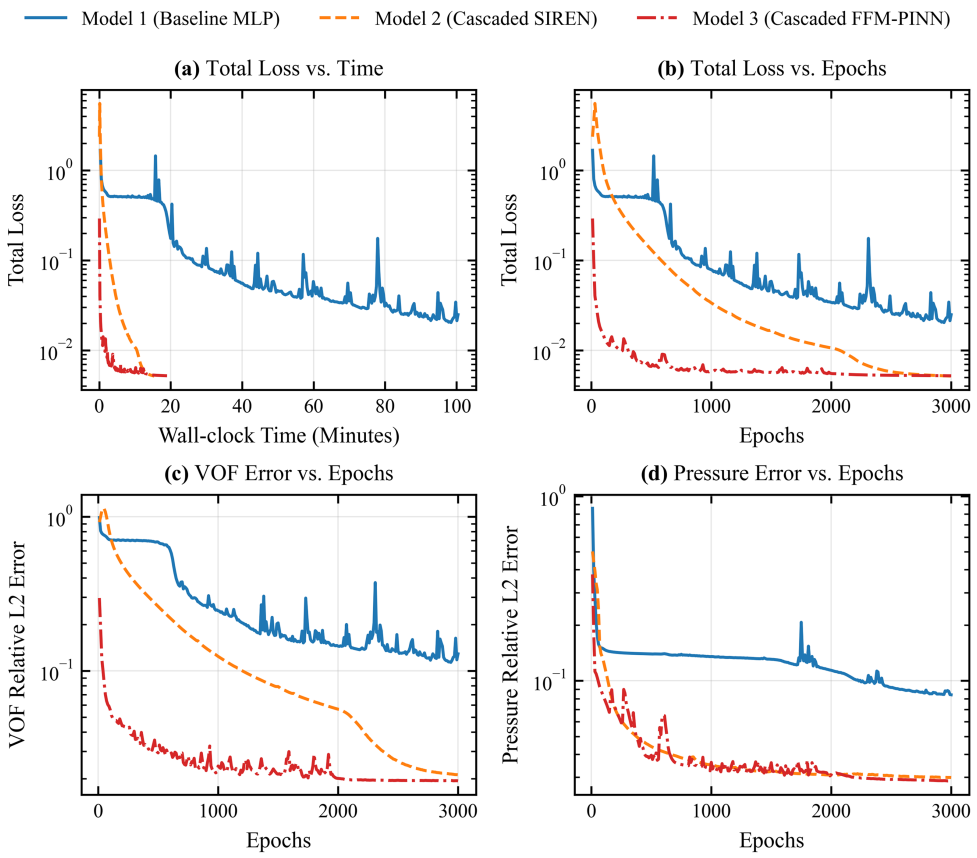


Figure 16: Training dynamics and convergence analysis of the three models. (**a**) Total loss vs. wall-clock time, demonstrating the significant acceleration of Model 3 (19 min) compared to Model 1 (100 min). (**b**) Total loss vs. epochs. (**c**,**d**) Evolution of relative L2 errors for the VOF and pressure fields, highlighting the rapid error decay and superior final accuracy achieved by the Cascaded FFM-PINN (Model 3) after transitioning to the L-BFGS optimizer at epoch 2000.

Furthermore, the evolution of relative L2 errors (Fig. 16c,d) highlights the effectiveness of the two-phase optimization strategy. Upon transitioning from the Adam optimizer to L-BFGS at epoch 2000, Model 3 experiences a sharp, monotonic decay in both error metrics. Ultimately, Model 3 suppresses the pressure and VOF relative L2 errors to exceptional levels of 2.87% and 1.93%, respectively. In contrast, Models 1 and 2 suffer from severe convergence stagnation and gradient conflicts, failing to achieve comparable high-fidelity interface localization.

4.2 Posterior Validation of Physical Consistency

To rigorously validate whether the surrogate models satisfy mass conservation and underlying physical laws, a posterior physical residual analysis was conducted on the predicted fields. Since Model 2 and Model 3 employ the identical physical constraint strategy (i.e., the gradient regularization in Eq. (11)), this section selects the baseline Model 1 (representing the full PDE constraint) and the optimal Model 3 (representing the proposed strategy) for an in-depth comparison.

Fig. 17 presents the histograms of the normalized physical residuals for both models, illustrating the flow field conservation characteristics under different physical constraint strategies. For Model 1, which explicitly enforces the full partial differential equation (PDE) constraints in the loss function, the residual distribution is extremely wide and exhibits a significant asymmetric shift. Specifically, the central 80% of the data for the continuity equation spans $[-2.3 \times 10^{-2}, 2.8 \times 10^{-2}]$, while the VOF advection equation spans a massive range of $[-1.0 \times 10^{-1}, 4.4 \times 10^{-1}]$. Residuals of this magnitude indicate severe systematic mass conservation violations. Mechanistically, forcing the full PDEs as soft constraints into the loss function triggers severe gradient flow pathologies and optimization conflicts during backpropagation, which prevents the network from converging to a physically conserved solution.

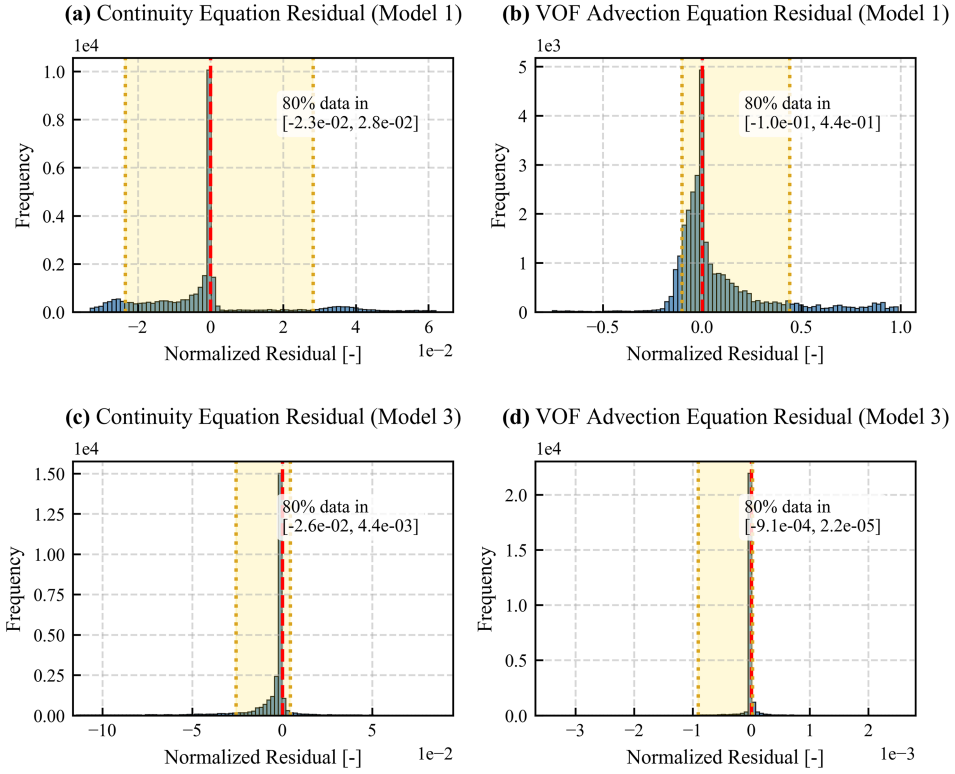


Figure 17: Histograms of the normalized physical residuals for Model 1 (full PDE constraint) and Model 3 (proposed strategy). The yellow shaded regions indicate the distribution range of the central 80% of the data.

In stark contrast, Model 3 demonstrates exceptional physical consistency achieved by the cascaded architecture and gradient regularization strategy. As shown in Fig. 17c,d, the residual distributions are highly concentrated near zero. While the lower bound of the continuity equation residual remains comparable to Model 1, its upper bound is significantly compressed to 4.4×10^{-3}, effectively suppressing the positive deviation. More importantly, the VOF advection equation residuals are drastically reduced to the 10^{-4} order of magnitude, strictly bounded within $[-9.1 \times 10^{-4},\ 2.2 \times 10^{-5}]$. Mechanistically, although Model 3 does not explicitly fit the full equations in the loss function, its cascaded architecture injects the physical causality of phase state determining physical properties as a strong inductive bias. Simultaneously, pure gradient regularization significantly smooths the loss landscape. This decoupled strategy successfully circumvents gradient conflicts under multi-field coupling, fundamentally ensuring exceptionally high physical fidelity and strict mass conservation.

4.3 Hyperparameter Sensitivity and Robustness

To comprehensively evaluate the robustness of the proposed cascaded FFM-PINN model, this section conducts sensitivity analyses on three critical hyperparameters: the spatio-temporal data sampling ratio, the VOF loss weight, and the random initialization of the FFM matrix. The quantitative results are summarized in Table 2.

(1) Spatio-temporal Sampling Ratio: The proposed 70%/30% (spatial/temporal) split was compared with 50%/50% and 90%/10% schemes. The results indicate that an excessive proportion of temporal data (50%/50%) compromises the spatial resolution of the phase interface, increasing the VOF error. Conversely, an insufficient temporal data ratio (90%/10%) fails to effectively capture the 10 Hz high-frequency pressure pulsations, causing the global pressure error to rise to 31.85%. The 70%/30% ratio achieves an optimal balance between spatial topology reconstruction and temporal dynamic tracking.

(2) VOF Loss Weight (λ_{vof}): The penalty weight in Eq. (9) was tested at values of 1.0, 10.0 (proposed), and 20.0. A small weight ($\lambda_{vof} = 1.0$) leads to severe numerical dissipation at the phase interface, increasing the VOF MSE by two orders of magnitude. An excessively large weight ($\lambda_{vof} = 20.0$) triggers gradient dominance in the loss function, severely inhibiting the convergence of the pressure field branch and causing the pressure error to surge to 42.15%. Therefore, $\lambda_{vof} = 10.0$ is a rational choice for the synergistic optimization of multiple physical fields.

(3) FFM Matrix Initialization: To verify the stability of the model's high-frequency perception, three different random seeds (Seed A, B, and C) were used to initialize the non-trainable FFM matrix **B**. The results show that the fluctuations in both VOF and pressure errors are minimal (<1.5%), indicating that the proposed architecture possesses excellent global optimization stability and reproducibility, independent of specific random initializations.

Table 2: Sensitivity analysis of critical hyperparameters on model accuracy.

Hyperparameter	Tested Values	VOF MSE	Pressure Rel. L_2 Error (%)
Data Split (Spatial/Temporal)	50%/50%	8.15×10^{-5}	14.31
	70%/30% (Proposed)	6.55×10^{-5}	2.87
	90%/10%	8.42×10^{-5}	31.85
VOF Loss Weight (λ_{vof})	1	5.21×10^{-3}	12.42
	10.0 (Proposed)	6.55×10^{-5}	2.87
	20	9.18×10^{-5}	42.15

(Continued)

Table 2 (continued)

Hyperparameter	Tested Values	VOF MSE	Pressure Rel. L_2 Error (%)
FFM Random Seed	Seed A	6.62×10^{-5}	2.91
	Seed B (Proposed)	6.55×10^{-5}	2.87
	Seed C	6.49×10^{-5}	2.84

4.4 Limitations and Future Perspectives

While the proposed framework achieves significant improvements in inference accuracy and computational efficiency, several limitations remain. First, the physical model assumes a homogeneous porous medium governed by the Kozeny-Carman equation. However, practical structural foundations exhibit high heterogeneity, such as fractured rock masses and stratified soils, which substantially alter multiphase flow trajectories. Second, the current surrogate model is trained and evaluated on a 2D symmetry plane to balance computational cost with proof-of-concept validation. Consequently, the reported inference time of 0.615 s is specific to this 2D resolution, and scaling the framework to full 3-D transient simulations will inevitably introduce exponentially higher degrees of freedom. Finally, the proposed FFM-PINN currently functions as an ultra-fast state synchronizer for real-time digital twins within a known time domain rather than an extrapolator for future unseen time steps. To address these constraints, future work will integrate operator learning techniques, such as Fourier Neural Operators and DeepONets [56–58], to process heterogeneous geological fields as functional inputs. This extension will ultimately support 3-D temporal-extrapolative predictions for complex underground engineering applications.

5 Conclusions

The simulation of variable-pressure pulsating grouting in porous media faces severe challenges, particularly the difficult reconstruction of strongly nonlinear multiphase flow interfaces and extremely time-consuming dynamic solving. To address these issues, this paper proposes a novel physics-guided cascaded neural network integrated with Fourier Feature Mapping (Cascaded FFM-PINN). The main conclusions are as follows:

(1) Algorithmic Architecture and Mechanistic Innovation: The framework innovatively embeds the physical causality logic—"phase determines physical properties, and properties dictate the flow field"—into a dual-branch cascaded architecture. By explicitly injecting the predicted volume fraction as a prior physical feature into the pressure network via a hard constraint, it effectively decouples strong multi-field nonlinearities. Furthermore, by employing a decoupled strategy of FFM and GELU, the model breaks the spectral bias of traditional networks while maintaining a smooth loss landscape.

(2) High-Fidelity Phase Interface Capture: The proposed model successfully overcomes the numerical smearing inherent in baseline networks (Model 1) and eradicates the non-physical high-frequency oscillations produced by SIREN-based networks (Model 2) in the mid-to-far field. It accurately identifies the phase field and sharp interfaces, reducing the global VOF MSE to an exceptionally low 6.55×10^{-5}, demonstrating superior spatial reconstruction capabilities.

(3) Dynamic Pressure Tracking and Stability: The model accurately captures the amplitude and phase of the 10 Hz pulsating pressure bubbles near the injection port. More importantly, unlike Model 2 which suffers from severe numerical noise in low-pressure regions, Model 3 perfectly suppresses far-field non-physical oscillations. This ensures global temporal robustness and reduces the overall relative pressure error to 2.87%.

(4) Millisecond-Level Inference and Computational Efficiency: The model achieves a paradigm shift from traditional CFD implicit iteration to data-driven forward inference. While maintaining high global statistical accuracy, it drastically compresses the single physical evolution time from 2.16×10^4 s (CFD) to 6.50×10^{-3} s. This successful realization of millisecond-level computation represents an acceleration of over six orders of magnitude.

(5) Limitations and Future Perspectives: Despite significant breakthroughs in inference accuracy and efficiency, the current model is constrained by fixed geological parameters (e.g., specific porosity and permeability). Future research will introduce Operator Learning (e.g., Fourier Neural Operator or DeepONet) to treat geological parameters as independent functional inputs, aiming to achieve generalized, high-fidelity, and rapid grouting simulations across complex and variable geological conditions.

Acknowledgement: The authors gratefully acknowledge the support of the Science and Technology Project of China Railway 25th Bureau Group Corporation Limited.

Funding Statement: The work described in this paper is fully supported by the Science and Technology Project of China Railway 25th Bureau Group Corporation Limited (Grant Number KF2025-078). The financial support is gratefully acknowledged.

Author Contributions: Weiqun Liang: Conceptualization, Methodology, Software, Investigation, Visualization, Formal analysis, Writing—original draft. Weiqin Xu: Methodology, Software, Validation, Formal analysis, Writing—review & editing. Xiaobin Chen: Conceptualization, Funding acquisition, Project administration, Supervision, Writing—review & editing. Qipei Han: Data curation. Yu Zhang: Visualization. Tiejie Xu: Investigation. Jiasheng Zhang: Supervision. All authors reviewed and approved the final version of the manuscript.

Availability of Data and Materials: The data that support the findings of this study are available within the article.

Ethics Approval: Not applicable.

Conflicts of Interest: The authors declare that this study received funding from China Railway 25th Bureau Group Corporation Limited. The funder was not involved in the study design, collection, analysis, interpretation of data, the writing of this article, or the decision to submit it for publication.

References

1. Liang W, Chen X, Tang L, Zhang J, Zhang X, Lin F, et al. Cement slurry penetration behavior of swirl grouting technology. Phys Fluids. 2024;36(9):095128. doi:10.1063/5.0225944.
2. Tang L, Chen X, Luo J, Zhang X, Zhu Z, Xie X, et al. Comprehensive study on the penetration behavior of cement slurry under high-frequency pulsating pressure. Phys Fluids. 2024;36(2):025161. doi:10.1063/5.0194313.
3. Tang L, Chen X, Zhang X, Wang Z, Wang Y, Xie K. Numerical analysis and experimental study on slurry diffusion characteristics of vortical oscillatory grouting technology considering soil interface. Phys Fluids. 2024;36(1):013313. doi:10.1063/5.0188294.
4. Delpisheh M, Ebrahimpour B, Fattahi A, Siavashi M, Mir H, Mashhadimoslem H, et al. Leveraging machine learning in porous media. J Mater Chem A. 2024;12(32):20717–82. doi:10.1039/d4ta00251b.
5. Hirt CW, Nichols BD. Volume of fluid (VOF) method for the dynamics of free boundaries. J Comput Phys. 1981;39(1):201–25. doi:10.1016/0021-9991(81)90145-5.
6. Jiang J. Simulating multiphase flow in fractured media with graph neural networks. Phys Fluids. 2024;36(2):023115. doi:10.1063/5.0189174.
7. Kapteyn MG, Pretorius JVR, Willcox KE. A probabilistic graphical model foundation for enabling predictive digital twins at scale. Nat Comput Sci. 2021;1(5):337–47. doi:10.1038/s43588-021-00069-0.
8. Brunton SL, Noack BR, Koumoutsakos P. Machine learning for fluid mechanics. Annu Rev Fluid Mech. 2020;52(1):477–508. doi:10.1146/annurev-fluid-010719-060214.

9. Jalota S, Wani SR, Rahimi I, Teshnizi ES, Tee KF. Prediction of cement take in Bakhtiari and Karun 4 dam foundation sites using ensemble machine learning algorithms. Transp Geotech. 2026;61(8):102073. doi:10.1016/j.trgeo.2026.102073.
10. Vinuesa R, Brunton SL. Enhancing computational fluid dynamics with machine learning. Nat Comput Sci. 2022;2(6):358–66. doi:10.1038/s43588-022-00264-7.
11. Zhao C, Zhang F, Lou W, Wang X, Yang J. A comprehensive review of advances in physics-informed neural networks and their applications in complex fluid dynamics. Phys Fluids. 2024;36(10):101301. doi:10.1063/5.0226562.
12. Raissi M, Perdikaris P, Karniadakis GE. Physics-informed neural networks: a deep learning framework for solving forward and inverse problems involving nonlinear partial differential equations. J Comput Phys. 2019;378:686–707. doi:10.1016/j.jcp.2018.10.045.
13. Karniadakis GE, Kevrekidis IG, Lu L, Perdikaris P, Wang S, Yang L. Physics-informed machine learning. Nat Rev Phys. 2021;3(6):422–40. doi:10.1038/s42254-021-00314-5.
14. Cai S, Mao Z, Wang Z, Yin M, Karniadakis GE. Physics-informed neural networks (PINNs) for fluid mechanics: a review. Acta Mech Sin. 2021;37(12):1727–38. doi:10.1007/s10409-021-01148-1.
15. Almajid MM, Abu-Al-Saud MO. Prediction of porous media fluid flow using physics informed neural networks. J Petrol Sci Eng. 2022;208(1):109205. doi:10.1016/j.petrol.2021.109205.
16. Alhubail A, Fahs M, Lehmann F, Hoteit H. Physics-informed neural networks for modeling flow in heterogeneous porous media: a decoupled pressure-velocity approach. In: Proceedings of the International Petroleum Technology Conference; 2024 Feb 12; Dhahran, Saudi Arabia. p. doi:10.2523/iptc-24362-ms.
17. Nguyen DTS, Palar PS, Zuhal LR, Duc ND, Duong VD. Darcy–Brinkman–Forchheimer physics-informed neural networks for inverse problems of homogeneous porous media flows. Phys Fluids. 2025;37(9):093626. doi:10.1063/5.0291172.
18. Ma M, Fu L, Guo X, Zhai Z. Incorporating lasso regression to physics-informed neural network for inverse PDE problem. Comput Model Eng Sci. 2024;141(1):385–99. doi:10.32604/cmes.2024.052585.
19. Patel P, Yadav SR. Physics informed neural networks simulation of fingering instabilities arising during immiscible and miscible multiphase flow in oil recovery processes. Chaos. 2025;35(7):073123. doi:10.1063/5.0273935.
20. Gong M, Zhang AM, Xiong C. Physics-informed neural networks for forward and inverse modeling of canonical interfacial instabilities of two-phase flows. Int J Multiph Flow. 2025;193(1):105368. doi:10.1016/j.ijmultiphaseflow.2025.105368.
21. Wang S, Yu X, Perdikaris P. When and why PINNs fail to train: a neural tangent kernel perspective. J Comput Phys. 2022;449(6481):110768. doi:10.1016/j.jcp.2021.110768.
22. Fuks O, Tchelepi HA. Limitations of physics informed machine learning for nonlinear two-phase transport in porous media. J Mach Learn Model Comput. 2020;1(1):19–37. doi:10.1615/jmachlearnmodelcomput.2020033905.
23. Wang S, Teng Y, Perdikaris P. Understanding and mitigating gradient flow pathologies in physics-informed neural networks. SIAM J Sci Comput. 2021;43(5):A3055–81. doi:10.1137/20M1318043.
24. McClenny LD, Braga-Neto UM. Self-adaptive physics-informed neural networks. J Comput Phys. 2023;474(3):111722. doi:10.1016/j.jcp.2022.111722.
25. Aminev D, Kravchenko M, Smirnov N. Improving PINN convergence in nonlinear multiphase flow problems through weight gradient consistency analysis. Mathematics. 2026;14(11):1832. doi:10.3390/math14111832.
26. Sitzmann V, Martel JNP, Bergman AW, Lindell DB, Wetzstein G. Implicit neural representations with periodic activation functions. Adv Neural Inf Process Syst. 2020;33:7462–73.
27. Wang S, Wang H, Perdikaris P. On the eigenvector bias of Fourier feature networks: from regression to solving multi-scale PDEs with physics-informed neural networks. Comput Meth Appl Mech Eng. 2021;384(1):113938. doi:10.1016/j.cma.2021.113938.
28. Hou BY, Bai YL, Jing XT, Huang CL. Fourier feature-enhanced multi-layer residual stacking network: a novel multiscale modeling approach for physics-informed neural networks. Neural Netw. 2026;195(31):108247. doi:10.1016/j.neunet.2025.108247.
29. Cheng S, Alkhalifah T. Multifrequency wavefield solutions for variable velocity models using meta-learning enhanced low-rank physics-informed neural network. Geophys J Int. 2025;244(1):ggaf417. doi:10.1093/gji/ggaf417.

30. Xu A, Liu Z, Rong H, Han L, Shi W, Huang J, et al. Structural optimization of a multi-story frame structure based on a pre-trained physics-informed neural network (PINN) surrogate model. Comput Model Eng Sci. 2026;147(1):1–10. doi:10.32604/cmes.2026.079375.
31. Peng R, Yang X. Recent advances in the application of porosity and permeability in porous media. Phys Fluids. 2025;37(7):076643. doi:10.1063/5.0271231.
32. Rehman M, Hafeez MB, Krawczuk M. A comprehensive review: applications of the Kozeny–Carman model in engineering with permeability dynamics. Arch Comput Meth Eng. 2024;31(7):3843–55. doi:10.1007/s11831-024-10094-7.
33. Feng D, Luo F, Chen B, Wang Y. Permeability prediction of porous media with non-circular pores using a modified Kozeny–Carman equation enhanced by fractal theory. Comput Geotech. 2026;193(1):107960. doi:10.1016/j.compgeo.2026.107960.
34. Standnes DC. Derivation of the conventional and a generalized form of Darcy's law from the Langevin equation. Transp Porous Medium. 2022;141(1):1–15. doi:10.1007/s11242-021-01707-x.
35. Zhang Z, Yan X, Liu P, Zhang K, Han R, Wang S. A physics-informed convolutional neural network for the simulation and prediction of two-phase Darcy flows in heterogeneous porous media. J Comput Phys. 2023;477(5):111919. doi:10.1016/j.jcp.2023.111919.
36. Tang L, Wang Z, Zhang X, Chen X, Luo J, Wang Y. Influence of rheological parameters on cement slurry penetration characteristics of novel oscillating grouting technology. Constr Build Mater. 2023;409(8):133999. doi:10.1016/j.conbuildmat.2023.133999.
37. Wu C, Zhu M, Tan Q, Kartha Y, Lu L. A comprehensive study of non-adaptive and residual-based adaptive sampling for physics-informed neural networks. Comput Meth Appl Mech Eng. 2023;403(6481):115671. doi:10.1016/j.cma.2022.115671.
38. Chai X, Cao W, Li J, Long H, Sun X. Overcoming the spectral bias problem of physics-informed neural networks in solving the frequency-domain acoustic wave equation. IEEE Trans Geosci Remote Sens. 2024;62(153):5923520. doi:10.1109/TGRS.2024.3440471.
39. Bin Waheed U. Kronecker neural networks overcome spectral bias for PINN-based wavefield computation. IEEE Geosci Remote Sens Lett. 2022;19:8029805. doi:10.1109/LGRS.2022.3209901.
40. Zhang L, Zhang X, Han S, Cong L, Wei Z. Enhancing frequency response in implicit full waveform inversion via Fourier encoding. IEEE Trans Geosci Remote Sens. 2026;64:5907921. doi:10.1109/TGRS.2026.3684378.
41. Lu L, Pestourie R, Yao W, Wang Z, Verdugo F, Johnson SG. Physics-informed neural networks with hard constraints for inverse design. SIAM J Sci Comput. 2021;43(6):B1105–32. doi:10.1137/21m1397908.
42. Sukumar N, Srivastava A. Exact imposition of boundary conditions with distance functions in physics-informed deep neural networks. Comput Meth Appl Mech Eng. 2022;389(5):114333. doi:10.1016/j.cma.2021.114333.
43. Tiwari N, Raghavamsi RVBS, Khare S, Shin B. Mitigating spectral bias in physics-informed neural networks through short-time Fourier transform synthesis for viscoelastic modeling. Comput Geotech. 2026;197(4):108180. doi:10.1016/j.compgeo.2026.108180.
44. Liu Y, Gu H, Yu X, Qin P. Diminishing spectral bias in physics-informed neural networks using spatially-adaptive Fourier feature encoding. Neural Netw. 2025;182(12):106886. doi:10.1016/j.neunet.2024.106886.
45. Xiong X, Lu K, Zhang Z, Zeng Z, Zhou S, Hu R, et al. High-frequency flow field super-resolution via physics-informed hierarchical adaptive fourier feature networks. Phys Fluids. 2025;37(9):097111. doi:10.1063/5.0286561.
46. Jagtap AD, Kawaguchi K, Em Karniadakis G. Locally adaptive activation functions with slope recovery for deep and physics-informed neural networks. Proc Math Phys Eng Sci. 2020;476(2239):20200334. doi:10.1098/rspa.2020.0334.
47. Xiang Z, Peng W, Liu X, Yao W. Self-adaptive loss balanced physics-informed neural networks. Neurocomputing. 2022;496(2):11–34. doi:10.1016/j.neucom.2022.05.015.
48. Hou X, Zhou X, Liu Y. Reconstruction of ship propeller wake field based on self-adaptive loss balanced physics-informed neural networks. Ocean Eng. 2024;309(1):118341. doi:10.1016/j.oceaneng.2024.118341.
49. Han C, He X, Wang Z, Fu Y. A self-adaptive physics-informed neural network for real-time prediction of structural damage. Mech Syst Signal Process. 2025;239(5):113322. doi:10.1016/j.ymssp.2025.113322.

50. Yu J, Lu L, Meng X, Karniadakis GE. Gradient-enhanced physics-informed neural networks for forward and inverse PDE problems. Comput Meth Appl Mech Eng. 2022;393(6):114823. doi:10.1016/j.cma.2022.114823.
51. Yan B, Harp DR, Chen B, Pawar R. A physics-constrained deep learning model for simulating multiphase flow in 3D heterogeneous porous media. Fuel. 2022;313(1):122693. doi:10.1016/j.fuel.2021.122693.
52. Jalili D, Jang S, Jadidi M, Giustini G, Keshmiri A, Mahmoudi Y. Physics-informed neural networks for heat transfer prediction in two-phase flows. Int J Heat Mass Transf. 2024;221(1):125089. doi:10.1016/j.ijheatmasstransfer.2023.125089.
53. Wessels H, Weißenfels C, Wriggers P. The neural particle method–an updated Lagrangian physics informed neural network for computational fluid dynamics. Comput Meth Appl Mech Eng. 2020;368(1):113127. doi:10.1016/j.cma.2020.113127.
54. Zhang J, Zhao X. Digital twin of wind farms via physics-informed deep learning. Energy Convers Manag. 2023;293(4):117507. doi:10.1016/j.enconman.2023.117507.
55. Wang M, Wang H, Yin Y, Rahardja S, Qu Z. Temperature field prediction for various porous media considering variable boundary conditions using deep learning method. Int Commun Heat Mass Transf. 2022;132(1):105916. doi:10.1016/j.icheatmasstransfer.2022.105916.
56. Jain N, Roy S, Kodamana H, Nair P. Scaling the predictions of multiphase flow through porous media using operator learning. Chem Eng J. 2025;503(24):157671. doi:10.1016/j.cej.2024.157671.
57. Lin R, Song T, Li J. Feature attention-based deep neural operator for solving seepage flow equations in porous media reservoir simulation. Phys Fluids. 2025;37(6):067152. doi:10.1063/5.0272866.
58. Liu Z, Archibong G, Bin Waheed U, Wang S, Song C. Physics-Informed Fourier-DeepONet for a generalized eikonal solution. Comput Geosci. 2026;206(1):106026. doi:10.1016/j.cageo.2025.106026.